

NAVAL POSTGRADUATE SCHOOL

Monterey, California



THESIS

**FEASIBILITY OF SCRAMJET TECHNOLOGY FOR AN
INTERMEDIATE PROPULSIVE STAGE OF AN
EXPENDABLE LAUNCH VEHICLE**

by

Michael D. Schafer

September 2002

Thesis Advisor:

Stephen Whitmore

Second Reader:

Charles Racoosin

Approved for public release; distribution is unlimited

THIS PAGE INTENTIONALLY LEFT BLANK

REPORT DOCUMENTATION PAGE			<i>Form Approved OMB No. 0704-0188</i>	
Public reporting burden for this collection of information is estimated to average 1 hour per response, including the time for reviewing instruction, searching existing data sources, gathering and maintaining the data needed, and completing and reviewing the collection of information. Send comments regarding this burden estimate or any other aspect of this collection of information, including suggestions for reducing this burden, to Washington headquarters Services, Directorate for Information Operations and Reports, 1215 Jefferson Davis Highway, Suite 1204, Arlington, VA 22202-4302, and to the Office of Management and Budget, Paperwork Reduction Project (0704-0188) Washington DC 20503.				
1. AGENCY USE ONLY (Leave blank)		2. REPORT DATE September 2002	3. REPORT TYPE AND DATES COVERED Master's Thesis	
4. TITLE AND SUBTITLE: Feasibility of SCRAMJET Technology for an Intermediate Propulsive Stage of an Expendable Launch Vehicle			5. FUNDING NUMBERS	
6. AUTHOR(S) Michael D. Schafer				
7. PERFORMING ORGANIZATION NAME(S) AND ADDRESS(ES) Naval Postgraduate School Monterey, CA 93943-5000			8. PERFORMING ORGANIZATION REPORT NUMBER	
9. SPONSORING /MONITORING AGENCY NAME(S) AND ADDRESS(ES) N/A			10. SPONSORING/MONITORING AGENCY REPORT NUMBER	
11. SUPPLEMENTARY NOTES The views expressed in this thesis are those of the author and do not reflect the official policy or position of the Department of Defense or the U.S. Government.				
12a. DISTRIBUTION / AVAILABILITY STATEMENT Approved for public release; distribution unlimited			12b. DISTRIBUTION CODE	
13. ABSTRACT (maximum 200 words) <p>The single largest contributor to the cost of putting objects into space is that of the launch portion. The currently available chemical rockets are only capable of specific impulse (Isp) values on the average of 300-350 seconds, with a maximum of 450 seconds. In order to improve the performance of the current families of launch vehicles, it is necessary to increase the performance of the rocket motors, and conversely the amount of propellant/oxidizer carried.</p> <p>The purpose of this thesis was to determine the feasibility of employing SCRAMJET technology for an intermediate propulsive stage of an expendable launch vehicle. This was motivated by the fact that SCRAMJETS offer a very high propulsive efficiency when compared to conventional chemical rockets. The incorporation of a SCRAMJET engine into the configuration "stack" of an expendable launch vehicle, offers the promise of increased payload mass fraction or an increase in the number of attainable orbital profiles. Analytical tools were developed using open-source software to identify launch trajectories for the SCRAMJET-enabled rocket configurations, and to determine how these would differ from conventional launch profiles. The effects of incremental increases in configuration lift and drag coefficients due to the SCRAMJET stage was analyzed. It was determined that incorporation of SCRAMJET Technology into an expendable rocket configuration offered marked improvement in performance, reduction in total launch weight, and increase operational flexibility when compared to a similarly sized conventional chemical rocket.</p>				
14. SUBJECT TERMS Launch Vehicle, SCRAMJET, pressure gradient, launch profile, launch trajectory, lift, drag, efficiency, intermediate stage propulsion			15. NUMBER OF PAGES 119	
			16. PRICE CODE	
17. SECURITY CLASSIFICATION OF REPORT Unclassified	18. SECURITY CLASSIFICATION OF THIS PAGE Unclassified	19. SECURITY CLASSIFICATION OF ABSTRACT Unclassified	20. LIMITATION OF ABSTRACT UL	

THIS PAGE INTENTIONALLY LEFT BLANK

Approved for public release; distribution is unlimited

**FEASIBILITY OF SCRAMJET TECHNOLOGY FOR AN INTERMEDIATE
PROPULSIVE STAGE OF AN EXPENDABLE LAUNCH VEHICLE**

Michael D. Schafer
Lieutenant, United States Navy
B.S., Oregon State University, 1992

Submitted in partial fulfillment of the
requirements for the degree of

MASTER OF SCIENCE IN SPACE SYSTEMS OPERATIONS

from the

**NAVAL POSTGRADUATE SCHOOL
September 2002**

Author: Michael D. Schafer

Approved by: Stephen A. Whitmore
Thesis Advisor

Charles M. Racoosin
Second Reader

Rudolf Panholzer
Chairman
Space Systems Academic Group

THIS PAGE INTENTIONALLY LEFT BLANK

ABSTRACT

The single largest contributor to the cost of putting objects into space is that of the launch portion. The currently available chemical rockets are only capable of specific impulse (I_{sp}) values on the average of 300-350 seconds, with a maximum of 450 seconds. In order to improve the performance of the current families of launch vehicles, it is necessary to increase the performance of the rocket motors, and conversely the amount of propellant/oxidizer carried.

The purpose of this thesis was to determine the feasibility of employing SCRAMJET technology for an intermediate propulsive stage of an expendable launch vehicle. This was motivated by the fact that SCRAMJETS offer a very high propulsive efficiency when compared to conventional chemical rockets. The incorporation of a SCRAMJET engine into the configuration “stack” of an expendable launch vehicle, offers the promise of increased payload mass fraction or an increase in the number of attainable orbital profiles. Analytical tools were developed using open-source software to identify launch trajectories for the SCRAMJET-enabled rocket configurations, and to determine how these would differ from conventional launch profiles. The effects of incremental increases in configuration lift and drag coefficients due to the SCRAMJET stage was analyzed. It was determined that incorporation of SCRAMJET Technology into an expendable rocket configuration offered marked improvement in performance, reduction in total launch weight, and increase operational flexibility when compared to a similarly sized conventional chemical rocket.

THIS PAGE INTENTIONALLY LEFT BLANK

TABLE OF CONTENTS

I.	INTRODUCTION.....	1
A.	PURPOSE.....	1
B.	STRUCTURE.....	1
II.	CONCEPT REVIEW	3
A.	MOTION OF ROCKETS	3
B.	HIGH SPEED FLIGHT	5
C.	AIR-BREATHING ENGINES	7
1.	Advantages of Air-Breathing Designs	7
2.	Limitations	9
D.	LAUNCH ECONOMICS	9
1.	Introduction.....	9
2.	Microcosm Model.....	10
a.	Terms/Methods.....	10
b.	Comparison of Reusable/Expendable.....	11
c.	Conclusion.....	14
III.	CURRENT HYPERSONIC RESEARCH.....	15
A.	MOTIVATION FOR HYPERSONIC FLIGHT	15
B.	UNITED STATES HYPERSONIC RESEARCH.....	15
1.	Vehicles	15
2.	Weapons	17
a.	Fast Hawk.....	17
b.	SHMAC	17
C.	FOREIGN HYPERSONIC RESEARCH EFFORTS.....	18
1.	Australia.....	18
2.	China	19
3.	France.....	19
4.	Germany	19
5.	Japan.....	20
6.	Russia	20
IV.	LAUNCH SIMULATION	23
A.	INTRODUCTION.....	23
B.	EQUATIONS OF MOTION IN THE ORBITAL PLANE	24
1.	Position Vector	24
2.	Velocity Vector	25
C.	DYNAMIC EQUATIONS USED BY SIMULATION	26
1.	Orbital Energy	26
2.	Acceleration Vector.....	26
3.	Resolution of Forces.....	27
a.	Gravity.....	27
b.	Thrust.....	28

	<i>c. Aerodynamic Forces</i>	<i>28</i>
	<i>d. Vehicle Mass.....</i>	<i>29</i>
	4. Generalized Equations of Motion.....	29
D.	TRANSFORMATION FROM GAUSSIAN TO INERTIAL COORDINATE SYSTEMS	30
E.	ATMOSPHERIC MODEL	31
F.	DEVELOPMENT OF AERODYNAMIC DATA	31
	1. Software Programs	31
	<i>a. AeroCFD</i>	<i>32</i>
	<i>b. HyperCFD</i>	<i>33</i>
	2. Aerodynamic databases.....	33
	<i>a. Subsonic Data.....</i>	<i>34</i>
	<i>b. Supersonic Data.....</i>	<i>36</i>
G.	LABVIEW	37
	1. Front Panel	38
	2. Block Diagram.....	39
	3. Icon/Connector Panel	39
H.	DEVELOPMENT OF SIMULATION TOOL.....	40
	1. Front Panel Clusters	41
	<i>a. Setup Cluster</i>	<i>41</i>
	<i>b. Autopilot/Waypoint Cluster</i>	<i>41</i>
	<i>c. Dynamic Controls/Indications Cluster.....</i>	<i>42</i>
	2. Order of Execution.....	43
	<i>a. Sub-frame 0</i>	<i>44</i>
	<i>b. Sub-frame 2</i>	<i>46</i>
	<i>c. Sub-frame 5</i>	<i>47</i>
	3. Using Launch_sim_autopilot	48
	<i>a. Pegasus Launch System.....</i>	<i>48</i>
	<i>b. Launch Trajectory.....</i>	<i>50</i>
V.	ANALYSIS CASE STUDY.....	53
A.	METHODOLOGY	53
B.	INITIAL CONDITIONS.....	53
C.	ATLAS III.....	54
	1. Configuration Data	54
	2. Trajectory Design.....	55
	3. Highlights	56
	<i>a. Stage 1 Burnout</i>	<i>56</i>
	<i>b. Stage 2 Burnout</i>	<i>57</i>
	<i>c. Apogee Burn.....</i>	<i>57</i>
D.	ATLAS III-SCRAM.....	60
	1. Configuration Data	60
	2. Trajectory Design.....	61
	3. ISS Mission Highlights	62
	<i>a. Stage 1 Burnout</i>	<i>63</i>
	<i>b. Stage 2 Burnout</i>	<i>63</i>

c.	<i>Apogee Burn</i>	64
4.	LEO Mission Highlights	65
a.	<i>Stage 1 Burnout</i>	66
b.	<i>Stage 2 Burnout</i>	66
c.	<i>Apogee Burn</i>	67
E.	CONCLUSIONS	68
1.	Performance Basis.....	68
2.	Economic Basis.....	69
3.	Censere Universus	70
VI.	FUTURE WORK	71
A.	INTRO.....	71
B.	SCRAMJET DEVELOPMENT PROGRAM	71
VII.	SUMMARY	73
APPENDIX A.	DERIVATION OF ALGORITHMIC EQUATIONS	75
A.	DERIVATION OF CLASSIC ORBITAL ELEMENTS	75
1.	Semi-major Axis, a	75
2.	Eccentricity, e	76
3.	Inclination, i	76
4.	Right Ascension of the Ascending Node, W	77
5.	Argument of Perigee, w	78
6.	True Anomaly, n	78
B.	COORDINATE SYSTEM TRANSFORMATION	79
1.	Position Vector (Inertial Frame)	79
2.	Velocity Vector (Inertial Frame)	80
C.	ESTABLISHING INITIAL CONDITIONS.....	80
1.	Position Vector	80
2.	Velocity Vector	81
APPENDIX B.	COMPARISON OF ISS MISSION ATLAS III/ ATLAS III- SCRAM PERFORMANCE CHARACTERISTICS	83
A.	ATLAS III.....	83
B.	ATLAS III-SCRAM.....	83
APPENDIX C.	AERODYNAMIC DATA	85
A.	SUBSONIC	85
B.	SUPERSONIC	87
	LIST OF REFERENCES	89
	BIBLIOGRAPHY	93
	INITIAL DISTRIBUTION LIST	95

THIS PAGE INTENTIONALLY LEFT BLANK

LIST OF FIGURES

Figure 2.1 Rocket Equation	3
Figure 2.2 Specific Impulse vs. Propellant Required	5
Figure 2.3 Atmospheric Temperature Distribution.....	6
Figure 2.4 Subsonic Vs. Supersonic Flow	6
Figure 2.5 Characteristic Mach Waves	7
Figure 2.6 Propulsion Systems Comparison.....	8
Figure 2.7 Velocity/Altitude Profiles of Propulsion Designs	9
Figure 2.8 Microcosm Reusable vs. Expendable Launch Vehicle Cost Model.....	11
Figure 2.9 Expendable vs. Reusable Launch Cost Over Time	13
Figure 2.10 Expendable vs. Reusable Running Average Launch Cost	13
Figure 2.11 Cost per Launch vs. Average Launch Rate, 2001 to 2015	14
Figure 3.1 Pegasus/X-43 Launch Configuration	16
Figure 3.2 X-43 Mission Profile	16
Figure 3.3 Fast Hawk Vehicle Design	17
Figure 3.4 Hyshot Shock Tunnel Test	18
Figure 3.6 Variable-thrust Scramjet Design	19
Figure 3.7 Phase I/II HSFD Vehicle Deployment	20
Figure 3.8 Hypersonic Flying Laboratory, “Kholod”	21
Figure 4.1 Gaussian Coordinate System.....	23
Figure 4.2. Perifocal Coordinate System	24
Figure 4.3 Polar/Planar Views of the Orbital Plane	25
Figure 4.4 Gravity Force Diagram.....	27
Figure 4.5 Thrust Force Diagram.....	28
Figure 4.6 Vector Force Diagram	28
Figure 4.7 Classic Orbital Elements	30
Figure 4.8 COE/Inertial Coordinate System.....	31
Figure 4.9 AeroCFD Front Panel Screenshot	32
Figure 4.10 AeroCFD Plot Examples	32
Figure 4.11 Hyper CFD Front Panel.....	33
Figure 4.12 Hypersonic Similarity Approximations.....	33
Figure 4.13 Notional Launch Vehicle Design	34
Figure 4.14 Body Tube Design	35
Figure 4.15 Fin Design	35
Figure 4.16 Launch Configuration Subsonic Data Plot	36
Figure 4.17 Stage II Subsonic Data Plot.....	36
Figure 4.18 HyperCFD Body/Fin Design	36
Figure 4.19 Launch Configuration Supersonic Data Plot.....	37
Figure 4.20 Stage II Supersonic Data Plot	37
Figure 4.21 Control Palette/Front Panel	38
Figure 4.22 Example Block Diagram	39
Figure 4.23 Example of Connector Pane Wiring.....	40

Figure 4.24 Process Flow Diagram.....	40
Figure 4.25 Setup Cluster	42
Figure 4.26 Autopilot/Waypoint Control Cluster	42
Figure 4.27 Dynamic Controls/Indications Cluster	43
Figure 4.28 Orbital Plane/Geocentric Ground Trace	43
Figure 4.29 <i>Initial_Conditions.vi</i> Diagram	44
Figure 4.30 <i>Read_aero_data.vi</i>	44
Figure 4.31 Sub-frame 0 (Autopilot Calculations)	45
Figure 4.32 Sub-frame 1 (Propagate State Vector).....	46
Figure 4.33 Sub-frame 2(Launch Diagnostics).....	47
Figure 4.34 Sub-frame 5(Manage S/C Mass)	47
Figure 4.35 User Dialog Box.....	48
Figure 4.36 X-43 Launch Configuration	49
Figure 4.37 Propulsion Stage Data	49
Figure 4.38 Reagan Test Site	50
Figure 4.39 Autopilot/Waypoint Control Cluster	50
Figure 4.40 RTS Launch Trajectory (Default Aero).....	51
Figure 4.41 RTS Launch Trajectory (X-43 Aero)	51
Figure 5.1 Atlas III 1 st Stage Characteristics	53
Figure 5.2 Atlas III.....	54
Figure 5.3 Centaur Upper Stage	55
Figure 5.4 Atlas III ISS Service Trajectory	56
Figure 5.5 Autopilot Waypoint Values	56
Figure 5.6 Autopilot Weights/Initial Values.....	56
Figure 5.7 Atlas III Stage One Burnout	57
Figure 5.8 Atlas III Stage Two Burnout	57
Figure 5.9 Atlas III Apogee Altitude	58
Figure 5.10 Atlas III-SCRAM	60
Figure 5.11 Atlas III-SCRAM Trajectory.....	61
Figure 5.12 Autopilot Waypoint Values	62
Figure 5.13 Autopilot Weights/Initial Values.....	62
Figure 5.14 Stage One Propulsion Data.....	62
Figure 5.15 Stage Two Propulsion Data	63
Figure 5.16 ISS Mission Stage One Burnout	63
Figure 5.17 ISS Mission Stage Two Burnout	64
Figure 5.18 ISS Mission Apogee Altitude	64
Figure 5.19 Stage One Propulsion Data.....	65
Figure 5.20 Stage Two Propulsion Data	66
Figure 5.21 LEO Mission Stage One Burnout	66
Figure 5.22 LEO Mission Stage Two Burnout	67
Figure 5.23 LEO Mission Apogee Altitude	67
Figure A.1 Inclination.....	76
Figure A.2 Right Ascension of the Ascending Node.....	77
Figure A.3 Argument of Perigee.....	78
Figure A.4 XYZ Coordinate System	79

Figure A.5 Geocentric Launch Position.....	80
Figure A.6 Ellipsoidal Earth Model.....	81

THIS PAGE INTENTIONALLY LEFT BLANK

LIST OF TABLES

Table 2.1 Typical I_{sp} Values	4
Table 2.2 Comparison of Expendable vs. Reusable Launch Cost Factors	11
Table 4.1 VI Frame Functions	45
Table 5.1 Final Orbit Insertion Requirements	68
Table 5.2 Comparison of Launcher Characteristics.....	69
Table 6.1 AIM-54 (Phoenix) Characteristics	72
Table B.1 Atlas III Mass Properties.....	83
Table B.2 Atlas III Performance Characteristics	83
Table B.3 Atlas III-SCRAM Mass Properties	83
Table B.4 Atlas III-SCRAM Performance Characteristics	83
Table C.1 Stage I/II (No delta correction)	85
Table C.2 Stage II (With Fins).....	85
Table C.3 Stage II (No Fins)	86
Table C.4 Delta Calculation (B.2-B.3)	86
Table C.5 Launch Configuration (B.1+B.4)	86
Table C.6 Stage I/II (No Delta Correction)	87
Table C.7 Stage II (With Fins).....	87
Table C.8 Stage II (No Fins)	87
Table C.9 Delta Calculation (B.7-B.8)	87
Table C.10 Launch Configuration (B.6+B.9)	88

THIS PAGE INTENTIONALLY LEFT BLANK

GLOSSARY OF TERMS

AIAA	American Institute of Aeronautics and Astronautics
AKM	Apogee Kick Motor
AoA	Angle of Attack
BAMB	Bending Annular Missile Body
CFD	Computational Fluid Dynamics
CIAM	Central Institute of Aviation Motors
COE	Classic Orbital Element
DFRC	Dryden Flight Research Center
DOF	Degrees of Freedom
FAA	Federal Aviation Administration
FY00	Fiscal Year 2000
GRC	Goddard Research Center
GTO	Geosynchronous Transfer Orbit
HETE	High Energy Transfer Experiment
HFL	Hypersonic Flying Laboratory
ILS	International Launch Services
ISS	International Space Station
MEO	Medium Earth Orbit
NASA	National Aeronautics and Space Administration
NASDA	National Space Development Agency
NASP	National Aerospace Plane
OCA	Orbital Carrier Aircraft
RBCC	Rocket Based Combined Cycle
RTS	Reagan Test Site
SCRAMJET	Supersonic Combustion Ramjet
SHMAC	Standoff Hypersonic Missile w/ Attack Capability
TF ³	Test-Fly-Fix-Fly
TRL	Technology Readiness Level
US	United States
VI	Virtual Instrument
VLS	Vertical Launch System
WCOOA	West Coast Offshore Operating Area

THIS PAGE INTENTIONALLY LEFT BLANK

LIST OF CONSTANTS, SYMBOLS, AND UNITS

C_p	Pressure Coefficient $\left(\frac{lb}{ft^2} \right)$
\bar{F}	Force $\left(\frac{kg \cdot m}{sec^2} \right)$
g_0	Gravitational Acceleration at Sea Level $\left(9.81 \frac{m}{sec^2} \right)$
I_{sp}	Specific Impulse (sec)
M	Mach # (unit-less)
m_{dry}	Dry (structural) Mass (kg)
m_{final}	Final Mass (kg)
m_{fuel}	Fuel/Oxidizer Mass (kg)
m_{init}	Initial Mass (kg)
m_{pay}	Payload Mass (kg)
P_{mf}	Propellant Mass Fraction (unit-less)
q_{bar}	Barometric Pressure $\left(\frac{lb}{ft^2} \right)$
R_{orbit}	Orbital Radius (km)
U_{ex}	Exhaust Velocity $\left(\frac{km}{sec} \right)$
V_r	Radial Velocity $\left(\frac{km}{sec} \right)$
V_n	Tangential Velocity $\left(\frac{km}{sec} \right)$
ΔV	Velocity Change $\left(\frac{km}{sec} \right)$
i	Inclination (deg)
m	Earth Gravitational Constant $\left(3.986 \times 10^5 \frac{km^3}{sec^2} \right)$
Ω	Right Ascension of the Ascending Node (deg)
w	Argument of Perigee (deg)

THIS PAGE INTENTIONALLY LEFT BLANK

ACKNOWLEDGMENTS

The author would like to acknowledge the financial support of NASA, Team Hyper-X, for providing the funds to purchase software and hardware used during the course of this thesis. This work was performed under Contract MIPR EO5257D.

The author would also like to thank Code RA personnel at NASA Dryden Flight Research Center for their assistance during all research visits, Stephen Whitmore and Charles Racoosin for their guidance, and Nancy Sharrock for her help in resolving the numerous formatting questions that arose during the course of thesis processing.

THIS PAGE INTENTIONALLY LEFT BLANK

I. INTRODUCTION

A. PURPOSE

This thesis explores the feasibility of adapting supersonic combustion ramjet (SCRAMJET) technology for the purpose of improving the performance capabilities of future U.S. expendable launch vehicle families. This is motivated by the high propulsive efficiency of this type of rocket compared to the more conventional chemical variants. The objective is not to design an actual rocket system, but rather to use analysis to identify whether the inclusion of such technology would provide a cost-justified improvement over current design schema.

The focus here is primarily upon addressing the following questions: what is the maximum performance of current launch vehicle configurations; what are the effects of incremental SCRAMJET drag increases on the flight profile; how can SCRAMJET technology be applied to improve launch vehicle performance; what is the optimal flight profile for a launch vehicle with a SCRAMJET intermediate stage; how does this flight profile contrast with conventional launch profiles; and what possible missions would benefit from the use of such a launch vehicle design.

B. STRUCTURE

The thesis is split into seven sections: Concept Review, Current Hypersonic Research, Development of Aerodynamic Data, Development of the Simulation, Analysis, Future Work, and Summary of Results.

The Concept Review section provides a brief review of the physical principles associated with supersonic flight, launch vehicle performance, and orbital dynamics. This refresher is vital to the understanding of the material covered in the later sections. Accompanying appendices provide a more rigorous mathematical-based review.

The next section gives a current snap-shot of US and international efforts in pursuing SCRAMJET technology. Different countries are pursuing this technology not just as a means of obtaining solutions to the problem of more efficient, lower cost space

transportation, but also as a means of advanced weapons design. It is significant to note the cooperative nature of many of these efforts.

The development of the aerodynamic data necessitated the use of several software programs, namely AeroCFD, HyperCFD and Microsoft Excel. AeroCFD and HyperCFD from Apogee Components provided the means of creating aerodynamic rocket forms and generating the accompanying aerodynamic data. Microsoft Excel was used to compile the aero data into spreadsheet form, and was instrumental in the validation of the AeroCFD/HyperCFD data.

The development of the simulation model used during the course of this thesis also relied upon software from several vendors, and is comprised of open-source coding. The simulation model enables the operator to dynamically alter various environmental and launch vehicle parameters, and view these effects concurrently. Such a design approach facilitates a greater understanding of the dynamics of launch vehicle travel through the atmosphere.

The Analysis section contains the information obtained from the computer model and presents the conclusions drawn from this analysis.

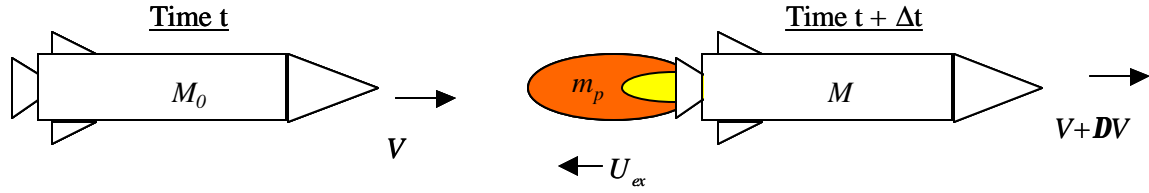
The Future Work section serves to identify points that were not addressed, or that arose during the course of thesis research, as well as points needing further investigation.

Finally, the Summary briefly reviews the tools and methods used during research, the results, and reiterates the motivation for applying SCRAMJET technology to launch vehicles, and the approaches used toward the goal of lower-cost, higher efficiency launch vehicle designs.

II. CONCEPT REVIEW

A. MOTION OF ROCKETS

When formulating his now famous equations of motion, Isaac Newton originally considered only the case where the mass of the system was conserved. His Second Law is also applicable where the mass of the system is not conserved, as is the case with rocket systems. In order to develop a mathematics expression for the motion of a rocket, one must make use of differential equations. Tsiolkovsky's rocket equation is given in Figure 2.1, where



$$\frac{dV}{dt} = \left[\frac{\dot{m}_p}{M} \right] U_{ex} \quad \frac{dM}{dt} \equiv \dot{m}_p \quad M = M_0 - m_p \quad \Rightarrow \quad \Delta V = g_0 \cdot I_{sp} \cdot \ln \left(\frac{M_0}{M} \right)$$

Figure 2.1 Rocket Equation

M_0 is the initial mass at the start of the burn, m_p is the amount of propellant burned in time dt , \dot{m}_p is the rate of change of the rocket mass, and U_{ex} is the effective exhaust velocity of the rocket

A useful concept for evaluating the performance of any rocket design is specific impulse (I_{sp}). Specific impulse is a measure of the rocket engine's ability to deliver an impulse $\left(\int_0^t F \cdot dt \right)$ for a given amount of propellant, and is represented in units of seconds. By convention, the ratio of thrust to mass-flow is divided by the earth's gravitational constant (g_o) to give units of seconds. Instantaneously, $I_{sp} = \frac{\bar{F}}{\dot{m}_p}$. I_{sp} is indirectly related to the type of fuel/oxidizer used. Table 2.1 indicates typical I_{sp} values for different propulsion systems.

Fuel	Oxidizer	I_{sp} (sec)
Cryogenics (LH ₂)	Oxygen	440-460
Hypergolics (MMH)	Nitrogen Tetraoxide	260-290
Solids	Ammonium Perchlorate	270
Electric (Ion)	--	2,500-10k
Nuclear	--	10 ² -10 ³ k

Table 2.1 Typical I_{sp} Values

Electric propulsion systems can produce very high I_{sp} values, but do not achieve high thrust levels. Political, environmental, and technical concerns have limited the use of nuclear propulsion sources for all but a few deep space applications. Research into new fuel/oxidizer mixes will not likely result in a significant increase in I_{sp} . Except for experimental gasses, the maximum possible I_{sp} from chemical rockets has likely been attained. What remains to be pursued is a more efficient use of existing technologies. This is a primary motivation behind this thesis research effort.

The rocket equation can be manipulated in order to provide an expression for the amount of fuel and oxidizer necessary to achieve a particular velocity change (delta V).

$$M_{(fuel+oxidizer)} = \left[M_{dry} + M_{payload} \right] \left[e^{\left[\frac{\Delta V_{burn}}{g_o \cdot I_{sp}} \right]} - 1 \right] \quad (2.1)$$

Important to note is the exponential relationship of the propellant load to “delta V” (ΔV). Also, I_{sp} has a profound effect upon launch performance. As the efficiency of the rocket motor increases, the amount of fuel necessary to achieve the required ΔV drops significantly. Figure 2.2 provides a graphic depiction of I_{sp} versus required propellant to place a 1000kg payload in orbit. Engine I_{sp} for several different launch vehicles are indicated.

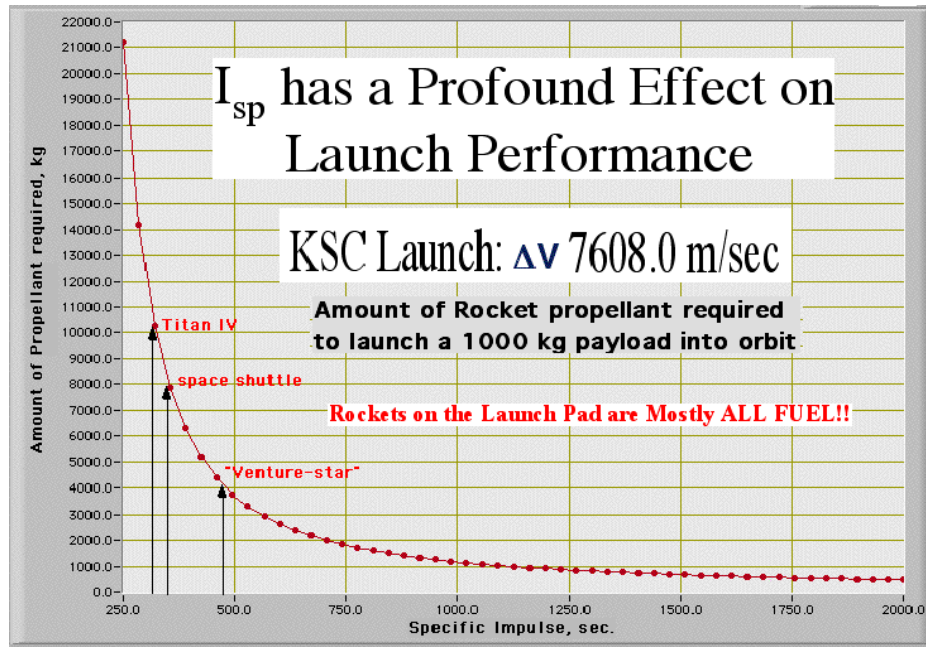


Figure 2.2 Specific Impulse vs. Propellant Required

Current engine designs have efficiencies to the left of the bend in the curve. If it is possible to get past this “knee”, a significant reduction of propellant carried is possible. Engines with an I_{sp} of 1000 would reduce the propellant required by the Shuttle, in order to loft a 1000kg payload, from the current 8:1 propellant mass-fraction (P_{mf}) to close to a 1:1 ratio.

B. HIGH SPEED FLIGHT

In order to have a meaningful discussion regarding the possible benefits of operating a launch vehicle in the atmosphere at much greater than the speed of sound, a common terminology must be agreed upon. A comparison between the characteristics of both subsonic and supersonic flight is also needed.

The speed of sound is the speed at which molecules communicate through pressure waves. This sound speed varies with altitude, as it is dependent upon the composition of the atmosphere through which it travels. Mach number (M) is a unit-less number that consists of a ratio between an object’s velocity (V) and the local sound speed (a).

$$M = \frac{V}{a} \quad (2.2)$$

The local sonic velocity is proportional to the temperature of the air. Figure 2.3 depicts how the temperature of the atmosphere varies with altitude. Flight is defined as supersonic for Mach numbers greater than 1.0, and hypersonic at Mach numbers greater than 5.

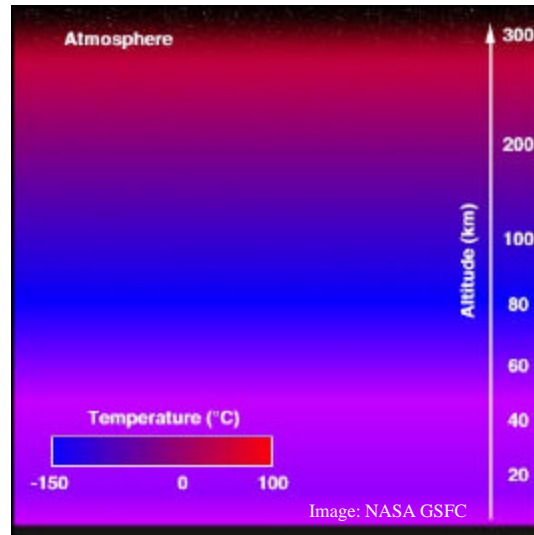


Figure 2.3 Atmospheric Temperature Distribution

An interesting aspect of supersonic flight defies common intuition. In supersonic flow, when area is restricted, air slows down; when area expands, the air speeds up. This is opposite from what occurs during subsonic flow. Figure 2.4 depicts the pressure velocity relationship for each case. The reason for this derives from the fact that air is compressible.

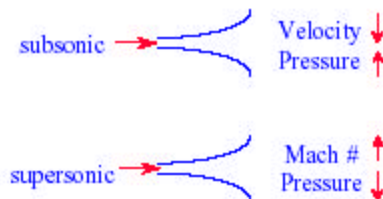


Figure 2.4 Subsonic Vs. Supersonic Flow

When a rocket collides with the atmosphere, the air compresses and changes in density (think of a traffic jam, with the cars as air molecules). This leads to the formation of a shock wave and causes a deflection in the path of the airflow. In subsonic flow the obstacle affects the flow upstream and downstream. In supersonic flow the obstacle is a hydrodynamic surprise and affects are only seen downstream; the upstream gas flows as

if the obstacle were not present. The angle these waves make with the body-plane of the disturbing body are a function of the body's Mach number, as depicted in Figure 2.5. A by-product of air-flow compression is thermal build up.

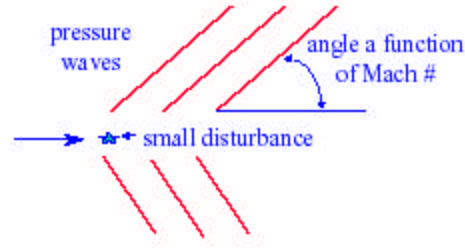


Figure 2.5 Characteristic Mach Waves

C. AIR-BREATHING ENGINES

The possibility that an air-breathing engine could be used to propel a vehicle into orbit was first envisioned almost four decades ago. It is only with recent advances in materials technology that serious consideration has been given towards these systems to facilitate access to space [\[McClinton\]](#).

1. Advantages of Air-Breathing Designs

There are several key advantages that air-breathing engines have over conventional rockets. Air-breathers utilize atmospheric oxygen instead of an onboard supply of oxidant, thus a smaller overall amount of fuel can be carried aboard the launch vehicle, thereby reducing weight, size and cost.

In a conventional rocket, the mass of oxidizer carried is about six times that of the required fuel. Rearranging the now familiar I_{sp} equation, we get an expression for I_{sp} in terms of propellant mass:

$$I_{sp} = \frac{F}{g_0 \dot{m}} = \frac{F}{g_0 [\dot{m}_{fuel} + \dot{m}_{ox}]} \approx \frac{F}{g_0 [\dot{m}_{fuel} + 6\dot{m}_{fuel}]} = \frac{F}{7g_0 [\dot{m}_{fuel}]} \quad (2.3)$$

By virtue of the fact that it does not need to carry an oxidizer supply, I_{sp} is increased by a factor of 7. The exact amount of increased efficiency is dependent upon the fuel mixture

used. Figure 2.6 gives a visual representation of the capabilities of current propulsion designs.

Another way of thinking about this is that an air-breathing engine, as compared to a rocket, uses approximately one-seventh the quantity of propellant in order to produce an equivalent amount of thrust. This allows for smaller, less costly designs, or the ability to get greater payloads to orbit for a given total weight. Air-breathing designs also offer increased operational flexibility compared to conventional rockets.

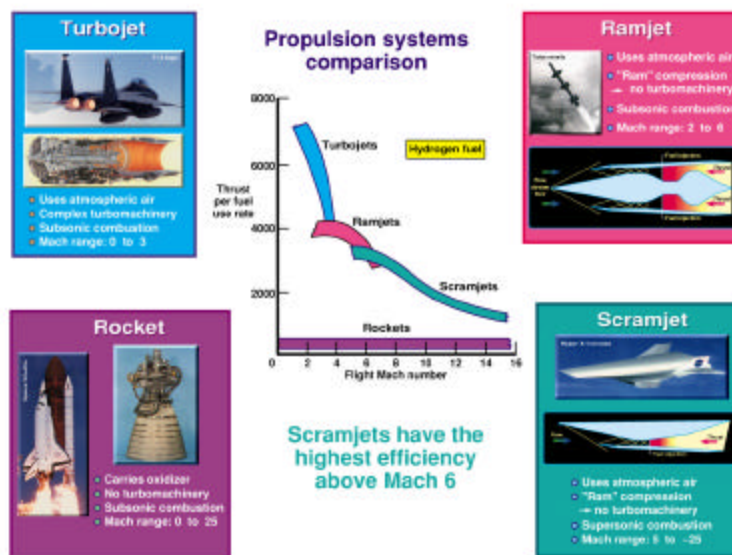


Image: Grif Corpening

Figure 2.6 Propulsion Systems Comparison

Hypersonic propulsion systems address the following NASA Aeronautics Technology objectives [[NASA GRC](#)]:

- Objective 6: Safety - Make space travel as safe as today's air travel. Reduce the incidence of crew loss by a factor of 40 by 2010 and by a factor of 100 by 2025.
- Objective 7: Cost - Reduce the cost of taking payloads to orbit. Reduce the cost of delivering a payload to Low Earth Orbit (LEO) by a factor of ten by 2010, and reduce the cost of inter-orbital transfer by a factor of ten by 2015. Reduce costs for both by an additional factor of ten by 2025.
- Objective 10: Technology Innovation - Develop the revolutionary technologies and technology solutions that enable fundamentally new aerospace system capabilities or new aerospace missions

It remains to be realized, but hypersonic propulsion has the potential to have as great an impact upon the way human beings live, work, and play as the advent of the airplane nearly 100 years ago.

2. Limitations

Air-breathing engines are not a miracle cure for the difficulties of launching objects into space. The engine inlet is designed to maintain airflow at a pre-determined velocity/pressure profile. There are distinct regions of the flight regime where air-breathing designs such as scramjets can operate efficiently. Supplemental propulsion systems, such as conventional rockets, must be used in order to place the scramjet system at the velocity/altitude profile at which the design can operate efficiently. Figure 2.7 depicts the velocity/altitude profiles where various propulsion designs could best be utilized.

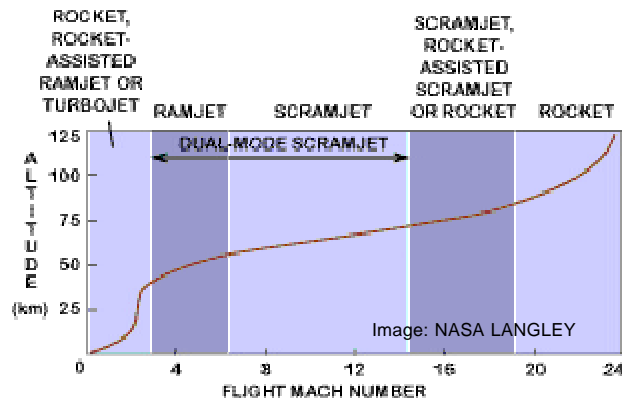


Figure 2.7 Velocity/Altitude Profiles of Propulsion Designs

Despite advances in many areas, the state of technology is still a limiting factor in the ability to field hypersonic designs. The upper speed limit of scramjets has yet to be determined, but it is envisioned that hypersonic designs are capable of attaining orbital velocities. At these extreme speeds, scramjets may no longer hold an advantage over rocket designs due to significant thermal and structural stresses.

D. LAUNCH ECONOMICS

1. Introduction

Irrespective of the performance capability of an individual class of launch vehicles, one is able to address their various associated costs in an effort to determine which has greater benefit than the other, and under what conditions these findings hold

true. The Microcosm Reusable Vs. Expendable Launch Vehicle Cost Model [Wertz] presented at the International Astronautics Federation Congress, in Rio de Janeiro Brazil, in October 2000 by James Wertz serves as the basis for determining the possible economic advantage/disadvantages of reusable/expendable launch vehicle designs. The following paragraphs will introduce the terminology and methods used by the Microcosm model, briefly present the model's economic comparison of reusable and expendable launch vehicles, and make use of these conclusions to address the feasibility of including scramjet technology within these designs.

2. Microcosm Model

a. Terms/Methods

Wertz begins his economic comparison of reusable and expendable launch vehicles with the following paragraph:

It is generally assumed by the community that reusable launch vehicles will dramatically reduce launch costs because you don't "throw away the vehicle" every time it is used. However, this is usually taken as an element of faith, without any substantive analysis to support the conclusion. The example of the Space Shuttle, originally sold to Congress on the basis of dramatically cutting launch costs, suggests that this conclusion might not be accurate under realistic conditions of development and operations.

What Wertz presented was an economic model that allows the comparison between the two different approaches. This in turn can be used to determine in what economic environment it is feasible to pursue reusability in whole or in part of the overall launch vehicle design.

The model developed by Wertz is presented in a purely analytic form. It was the goal of the author (Wertz) to "clearly separate the economic model from the conclusions based on using it." In this manner it is possible for different users to develop their own conclusion based upon their own experiences and assumptions. The total launch cost model is presented in Figure 2.8. All figures which depict launch costs are given in millions of FY00 dollars with an adjustment for inflation of 3%/yr. Complete derivation of the Microcosm model is beyond the scope of this thesis, and readers desiring a more thorough presentation of the economic model should refer to the source document.

$$C_{launch} = C_{development} + C_{vehicle} + C_{flightops} + C_{recovery} + C_{refurb} + C_{insurance}$$

Where:

C_{launch}	≡	Total cost of launch in FY00 dollars (excludes inflation)
$C_{development}$	≡	Amortization of nonrecurring development cost
$C_{vehicle}$	≡	Reusable: Amortization of vehicle production cost Expendable: Recurring production cost (Theoretical First Unit cost reduced by learning curve)
$C_{flightops}$	≡	Total cost of flight operations per flight
$C_{recovery}$	≡	Recurring cost of recovery (reusable only)
C_{refurb}	≡	Refurbishment cost (reusable only)
$C_{insurance}$	≡	Cost of launch insurance

Figure 2.8 Microcosm Reusable vs. Expendable Launch Vehicle Cost Model

b. Comparison of Reusable/Expendable

Table 2.2 summarizes the differences between expendable and reusable vehicles in the Microcosm model. Exp refers to an expendable vehicle and ReU refers to a reusable vehicle.

<i>Exp</i>	<i>ReU</i>	<i>Factor</i>	<i>Discussion</i>
X	X	Amortization of nonrecurring development cost	Higher for ReU due to larger nonrecurring
X	X	Exp: Recurring production cost ReU: Amortization of production cost	Exp uses learning curve; ReU is more complex and expensive to produce; <u>Amortization</u> rather than recurring production is the major ReU cost savings
	X	Recovery cost	0 for Exp
	X	Refurbishment cost	May be substantial for ReU; 0 for Exp
X	X	Flight operations	ReU has more complex systems; more expensive check-out and recovery
X	X	Vehicle insurance	Depends on both replacement cost and reliability; Exp or ReU could be cheaper

Table 2.2 Comparison of Expendable vs. Reusable Launch Cost Factors

Reusable vehicles enjoy the benefit of not throwing away expensive hardware every time the vehicle flies. At first glance, this might lead to the assumption that reusability is always the best course of development efforts. One must be careful not to fall into this psychological trap, as reusable vehicles tend to be more complex, robustly

built (possibly heavier) to withstand repeated use, and more expensive to develop. Components that are designed for use in vehicle recovery are of little use during the launch phase of operations. Likewise launch systems would be considered “dead weight” during the recovery phase (that is why the Shuttle jettisons it’s external tank). By virtue of their design philosophy, expendable vehicles enjoy a greater payload to gross lift-off weight ratio.

In addition to lower payload capacity, reusable vehicles incur the costs of recovery, refurbishment, and retesting/recertification. These are costs that are not borne by expendable designs. Another item to consider is the aging of a reusable vehicle fleet. Experience shows that as vehicles get older, more money has to be expended on maintenance efforts, necessitating greater testing and certification efforts. The current problems with the fuel flow liners plaguing the Shuttle fleet is a good example of what happens when your vehicles get older [[Shuttle](#)].

Figure 2.9 shows expendable vs. reusable launch costs over time. This most likely represents what the majority of launch vehicle manufacturers experience during the course of a launch vehicles useful lifetime. Cost per launch drops off for both reusable and expendable designs once the development costs are amortized. Important to note, is that for reusable vehicles, there will come a time when it will no longer be economically feasible to repair the vehicle, and a replacement must be sought. Currently, the Shuttle is the only vehicle design that can be considered reusable, and the age of the fleet is on the order of 20 years. Figure 2.10 shows expendable vs. reusable running average launch costs.

The running average approach addresses the need to develop a replacement vehicle around the 15-20 year point. It also prevents the steep drop in launch cost at this point evidenced in Figure 2.9. This prevents the situation of a customer delaying a vehicle launch until after year 15 in order to take advantage of the “perceived” drop in launch costs, when in fact such a course of action would reduce the launch rate and prevent amortization of the vehicles development. The fact that studies are still being conducted in an effort to select a replacement for the Shuttle suggests that the program managers did not budget for a Shuttle replacement during its development.

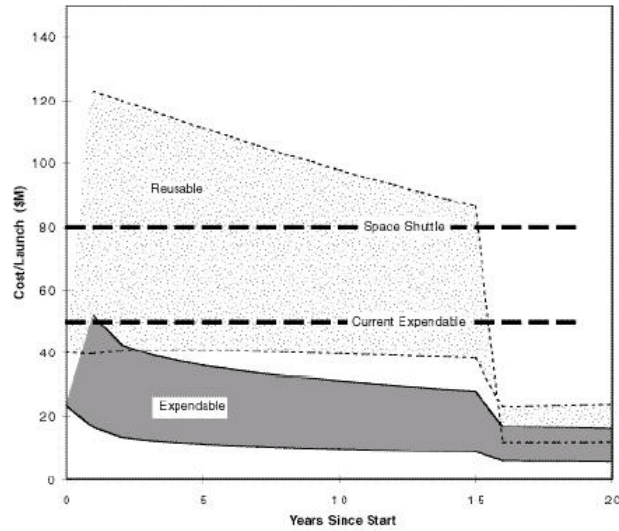


Figure 2.9 Expendable vs. Reusable Launch Cost Over Time

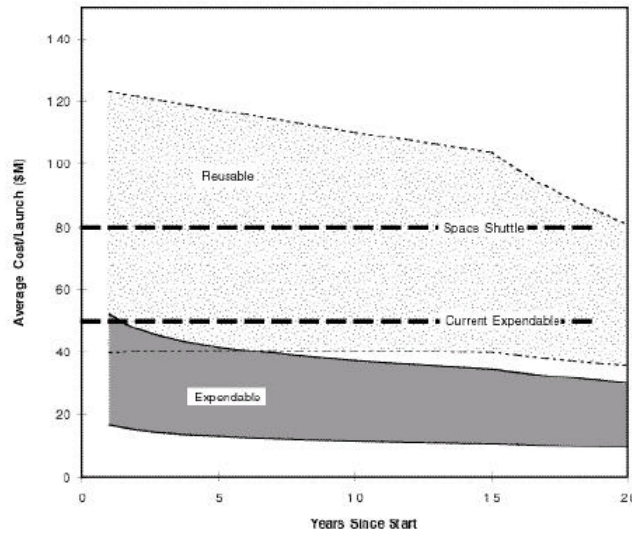


Figure 2.10 Expendable vs. Reusable Running Average Launch Cost

The biggest influence upon the cost of a launch vehicle is the number of launches that occur per year. Figure 2.11 gives the cost per launch vs. the average launch rate over a fifteen-year period from 2001-2015. The point to take away from the figure is that as the number of launches per year increases, the associated cost for each launch will decrease. This reduction in launch cost is enjoyed for both reusable and expendable vehicle designs.

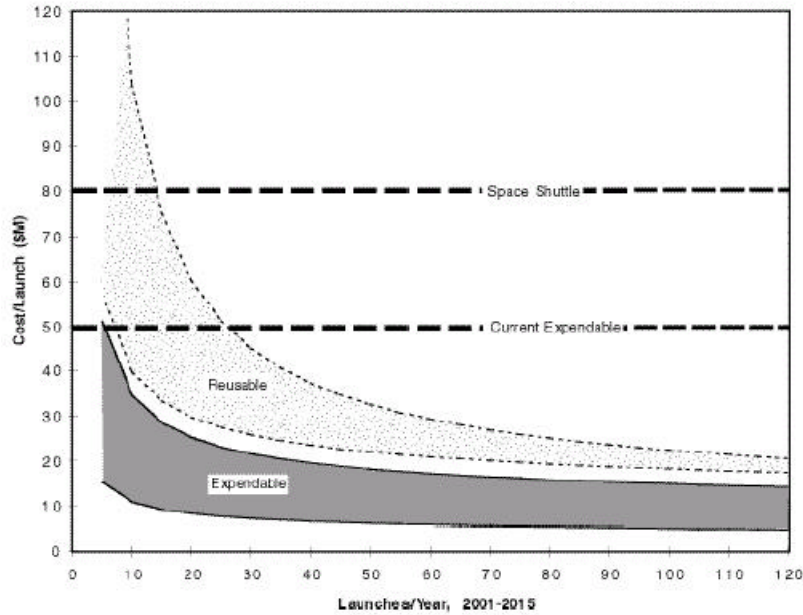


Figure 2.11 Cost per Launch vs. Average Launch Rate, 2001 to 2015

c. Conclusion

Wertz concludes that unless the launch rate is significantly greater than 100 vehicles per year, expendable vehicles will continue to enjoy a “significant economic advantage” over reusable vehicles. Assuming that the model costs are realized, a drop in expendable vehicle launch costs by a factor of 5-10 should be possible. This advantage is due in part to the fact that expendable vehicles do not have to account for recovery/refurbishment costs, are able to incorporate new technology and upgrades more easily than reusable designs, and that flight operations for expendable vehicles are in general less complex than for reusable vehicles.

Once it is accepted that expendable vehicles provide an economically viable means of delivering payloads to orbit, the question must be asked is it possible to improve further. Scramjet engines have potential I_{sp} values well to the right of the curve in Figure 2.2. If a scramjet is incorporated into the launch stack of an expendable design, there is the potential of reducing the total launch-mass of the vehicle by approximately half.

III. CURRENT HYPERSONIC RESEARCH

A. MOTIVATION FOR HYPERSONIC FLIGHT

The possibility that an air-breathing engine could be used to propel a vehicle into orbit was first envisioned almost four decades ago. As early as 1948, engineers at Dryden Flight Research Center were conducting flight tests with vehicles such as the Bell XS-1 at speeds greater than Mach 1. In 1952, preliminary studies were begun that attempted to address problems associated with spaceflight. The X-15, which holds the current world records for altitude and speed for winged aircraft, last flew in 1968. Despite several efforts, no usable hypersonic vehicle was developed for the next four decades. Dr. Richard P. Hallion, chief historian for the U.S. Air Force, observed that early hypersonic technology was in effect ahead of its time. Quoted in a 19 August 1997 *New York Times* article, Dr. Hallion commented [[CDISS](#)]:

When you look at the hypersonic work of the 50's and 60's, a lot of it was really very good, far in advance of its time. What was not advanced was the ability to develop the structures, materials, propulsion, guidance and controls to make operational vehicles based upon the research. We can contemplate vehicles today that are far more practical to develop than in the 1960's, when much of the pioneering work was done.

With recent advances in material science, designs that were once considered impractical may hold the key to providing cheaper access to space.

B. UNITED STATES HYPERSONIC RESEARCH

1. Vehicles

The United States current research efforts into hypersonic vehicles focus upon the X-43 series of vehicles, collectively dubbed “Hyper-X.” This program owes much of its legacy to the National Aerospace Plane (NASP). The NASP was supposed to demonstrate hypersonic-to-orbit flight, but was cancelled in 1993 [[Aerospaceguide](#)]. The Hyper-X test vehicles will be 12 ft (3.6 m) in length and have a wingspan of 5 ft (1.5 m). They will employ a hydrogen-fueled ramjet/scramjet. The Pegasus booster built by Orbital Sciences Corporation of Chandler, Arizona accelerates the X-43 to launch

velocity (Mach 7). The Pegasus and attached X-43 are carried aloft by NASA Dryden's B-52 "Mothership", depicted in Figure 3.1.



Figure 3.1 Pegasus/X-43 Launch Configuration

Figure 3.2 depicts the planned X-43 mission profile. Following release from the B-52 "Mothership," the Pegasus booster delivers the X-43 to test altitude and airspeed. Upon booster burnout, the X-43 enters free flight and the Scramjet engine ignites. Following the powered-flight portion of the test, the X-43 is maneuvered to dissipate speed/energy and arrive at the desired impact area.

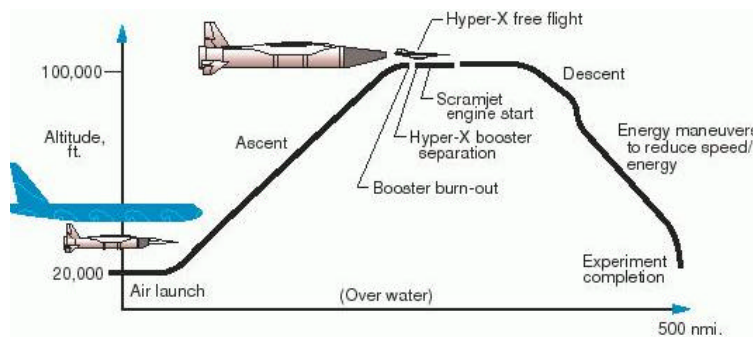


Figure 3.2 X-43 Mission Profile

The first flight of the X-43A occurred on June 2nd, 2001. Five seconds into flight, the Pegasus booster went out of control. Subsequently, Flight Controllers destroyed both vehicles [Edwards AFB]. NASA engineers are currently working with industry to refine the X-43 design. Two other variants of the X-43 are planned. The X-43C will be increased in length by four feet in order to accommodate its hydrocarbon fuel source. The X-43B will be a propulsion demonstrator for a rocket-based combined cycle (RBCC)

engine design. Unlike the X-43A/C variants, the X-43B will not need the Pegasus booster [Soppet]. It will be able to switch between rocket mode and scramjet modes of operation.

2. Weapons

a. *Fast Hawk*

In support of the Department of Defense's (DoD) Joint Warfighter Precision Force vision, the Office of Naval Research is sponsoring research into a hypersonic follow-on design to the Tomahawk cruise missile. The Low-Cost Missile ATD, commonly known as Fast Hawk, seeks to demonstrate a unique, finless, low-drag bending annular missile body (BAMB) airframe and ramjet propulsion concept to give the Navy the capability to attack time-critical and hardened targets [MILNET]. In this concept, depicted in Figure 3.3, the ramjet combustor and tandem booster are connected to the frontal missile airframe by an articulating thrust vector control joint.



Figure 3.3 Fast Hawk Vehicle Design

b. *SHMAC*

The Air Force's AF2025 study envisions a hypersonic attack missile as a critical component in ensuring the Air Force's ability to achieve Global Reach/Global Power [USAF]. The Standoff Hypersonic Missile with Attack Capability (SHMAC), is envisioned as a Mach 8 weapon driven by a combined rocket/scramjet (RBCC) propulsion system, capable of being launch from either aircraft, ship-based vertical launch system (VLS) tubes, or mobile or fixed ground sites. A modular payload design will allow for a maximum of flexibility in highly fluid future combat situations.

C. FOREIGN HYPERSONIC RESEARCH EFFORTS

Foreign efforts into hypersonic research can best be characterized as a multinational effort. No individual country has the economic might to individually challenge the United States. In view of the current austere budgetary environment, even the US is beginning to adopt such a cooperative development arrangement.

1. Australia

Australia leads a multinational hypersonic flight project involving personnel from Great Britain, Germany, South Korea, Japan, and the United States. HyShot is the University of Queensland initiative that seeks to establish a correlation between pressure measurements of an axis-symmetric scramjet design made in the University of Queensland T4 shock tunnel (Figure 3.4) and those actually experienced in flight. The

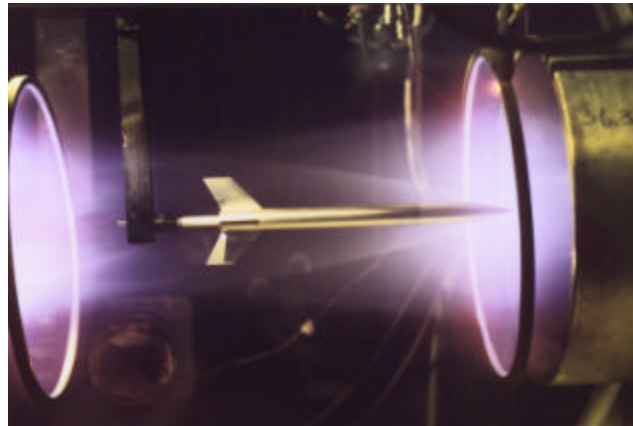


Figure 3.4 Hyshot Shock Tunnel Test

HyShot Program uses a two-stage Terrier-Orion Mk70 rocket to boost the payload and the empty Orion motor (the Orion motor remains attached to the payload) to an apogee of approximately 330km. As the spent motor and its attached payload fall back to Earth, they gather speed, and the trajectory is designed so that between 35km and 23km, they are traveling at Mach 7.6 [[HYSHOT](#)].

The HyShot Program secured its place in history with the first successful flight test of supersonic combustion [[History](#)]. Future flight trials will seek to develop an engine design with a net positive thrust.

2. China

Information regarding China's hypersonic program is extremely sparse. A September 17, 2001 news article stated that Chinese researchers were currently working on an aircraft capable of flying at five times the speed of sound. The Xinhua news agency quotes the Chinese Academy of Science as saying, "A Chinese 'hypersonic' aircraft, able to cover 6,105 kilometers an hour, could be developed in 10 to 15 years [[Airwise](#)]."

3. France

France is a recognized leader in high-speed engine design. They currently field a ramjet-propelled cruise missile (ASMP) capable of Mach 3.5, with plans for a follow-on version capable of Mach 5+ [[CDISS](#)]. France entered into a partnership with the Moscow Aviation Institute in 1995. The goal of the partnership is to produce a variable-thrust scramjet engine, depicted in Figure 3.6, with performance in the Mach 2-12 range. The tests are similar to those being performed by NASA's Hyper-X program.

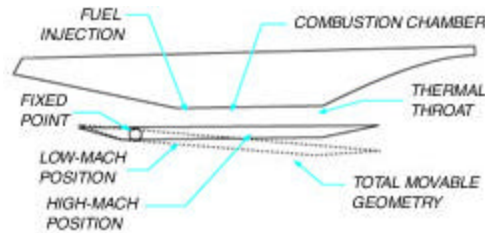


Figure 3.6 Variable-thrust Scramjet Design

France has also engaged in joint research with Germany to develop a hypersonic surface to air missile for air defense purposes, and will cooperate with Japan's National Space Development Agency (NASDA) to conduct the flight-testing of the Japanese unmanned shuttle design, dubbed HOPE-X.

4. Germany

Germany has recently tested flown a hypersonic experimental missile (HFK), reaching speeds of greater than Mach 6 [[Jane's Missiles and Rockets](#)]. The test established the performance of a conical-shaped engine designed by the French Corporation EADS. EADS/LFK chief executive officer Werner Kaltenegger said, "Using the hypersonic test bed, we are able to investigate a broad variety of technical and physical phenomena in the high-speed range which will be of advantage to future applications." Further flight-testing of the HFK is expected to occur in 2003.

5. Japan

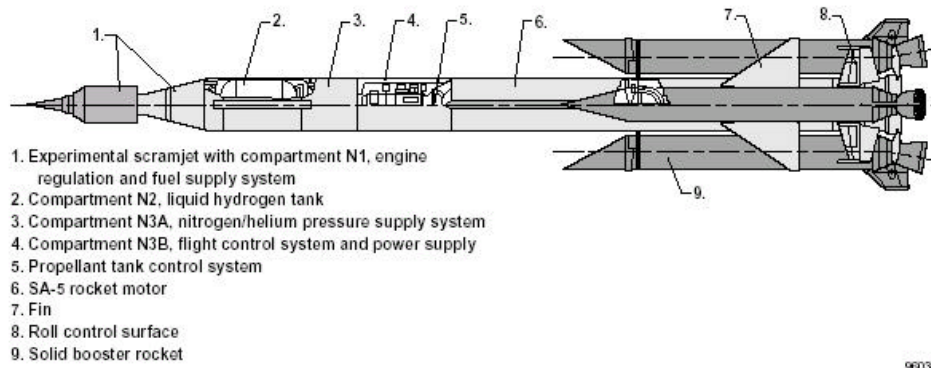
Japan has entered into an agreement with the French Space Agency (CNES) to conduct high-speed flight tests, as a part of Japan's H-II Orbiting Plane Experiment (HOPE-X) program, to develop a reusable space transportation system [\[CNES-NASDA\]](#). The two-phase High-Speed Flight Demonstration ([HSFD](#)) program is scheduled to begin in 2002. The first phase of the program will use a jet engine powered flight vehicle to verify the autonomous landing system design. Phase II will validate the aerodynamic tools used to predict vehicle-handling characteristics during transonic flight, using a 25% scale model (Figure 3.7) of the HOPE-X vehicle dropped from a stratospheric balloon. Both experiments will be performed at the Esrange test site in Sweden.



Figure 3.7 Phase I/II HSFD Vehicle Deployment

6. Russia

In the 1990s, the Russians began conducting tests of hydrogen-fueled ramjet/scramjet engines as part of a high-speed flight program. In November 1994, Russia's Central Institute of Aviation Motors (CIAM) entered into a partnership with NASA in an effort to determine the maximum Mach number at which a scramjet can be expected to operate [\[AIAA-96-4572\]](#). The Hypersonic Flying Laboratory (HFL), "Kholod," shown in Figure 3.8 below, carries aloft this axisymmetric scramjet design. On February 12, 1998, a launch was conducted at the Sary Shagan test range in central Kazakhstan. During the test, the HFL achieve a maximum velocity greater than Mach 6.4 [\[NASA/TP-1998-206548\]](#).



960357

Figure 3.8 Hypersonic Flying Laboratory, “Kholod”

THIS PAGE INTENTIONALLY LEFT BLANK

IV. LAUNCH SIMULATION

A. INTRODUCTION

As part of this thesis, it was necessary to develop a method of simulating a rocket launch. The goal was to be able to take a snapshot of the dynamic conditions experienced by the launch vehicle at any point in time. The end product is 3 degree of freedom (DOF) simulation, which models radial velocity (V_r), tangential velocity (V_n), radius (r), true anomaly (θ), and mass (m). The differential equations used to describe the orbital motion of the spacecraft are derived using the *satellite* or *Gaussian* coordinate system [Vallado]. In this coordinate system, the *r-component* points away from the center of the Earth in a radial direction, the *n-component* is perpendicular to the radial direction and points in the direction of travel of the spacecraft, and the *l-component* completes the right-handed orthogonal coordinate system. This coordinate system stays fixed to the spacecraft at all times, and the *l-component* is always perpendicular to the instantaneous orbit. The Gaussian coordinate system is depicted in Figure 4.1.

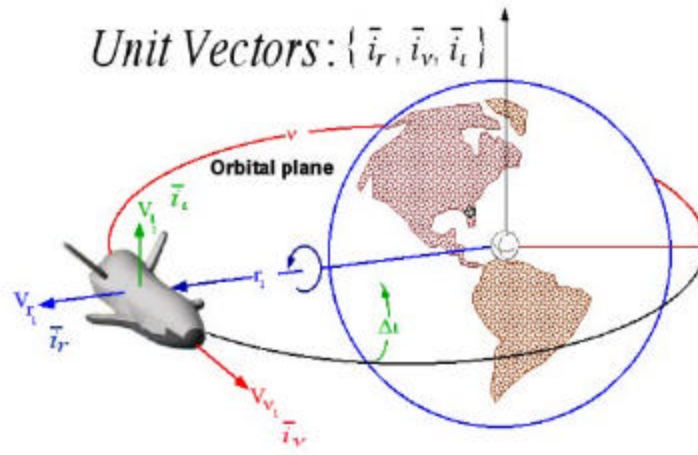


Figure 4.1 Gaussian Coordinate System

The National Instruments software program LabVIEW was used to code the launch simulator. LabVIEW operates on the principle of data flow, vice traditional top-down software design methodologies. This approach enables the user to create virtual instruments with little or no programming language experience.

B. EQUATIONS OF MOTION IN THE ORBITAL PLANE

Figure 4.2 depicts the Perifocal Coordinate System used in establishing the equations of motion. True anomaly, \mathbf{n} , describes the orbital position of the vehicle with respect to perigee (covered further in section B).

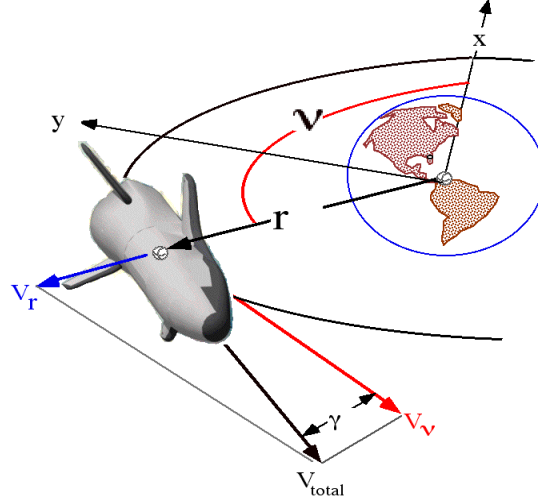


Figure 4.2. Perifocal Coordinate System

1. Position Vector

The polar form of the position vector, \bar{R} , is represented by

$$\bar{R} = \begin{bmatrix} R \\ 0 \\ 0 \end{bmatrix} \quad (4.1)$$

The Cartesian form of the position vector is

$$\begin{bmatrix} R_x \\ R_y \\ R_z \end{bmatrix} = \begin{bmatrix} r \cos(\mathbf{n}) \\ r \sin(\mathbf{n}) \\ 0 \end{bmatrix} \quad (4.2)$$

The orbital radius can also be described in terms of the equation of an ellipse

$$R = \frac{a[1 - e^2]}{1 + e \cos(\mathbf{n})} \quad (4.3)$$

2. Velocity Vector

The velocity vector, \vec{V} , has both radial and tangential components represented as

$$\vec{V} = \begin{bmatrix} V_r \\ V_n \\ 0 \end{bmatrix} \quad (4.4)$$

where:

g = vehicle flight path angle (deg)

$$V_r = \|\vec{V}\| \sin(g) \quad (4.5)$$

$$V_n = \|\vec{V}\| \cos(g) \quad (4.6)$$

The Cartesian form of the velocity vector is

$$\begin{bmatrix} V_x \\ V_y \\ V_z \end{bmatrix} = \begin{bmatrix} \cos(n) & -\sin(n) & 0 \\ \sin(n) & \cos(n) & 0 \\ 0 & 0 & 1 \end{bmatrix} \begin{bmatrix} V_r \\ V_n \\ 0 \end{bmatrix} = \begin{bmatrix} V_r \cos(n) - V_n \sin(n) \\ V_r \sin(n) + V_n \cos(n) \\ 0 \end{bmatrix} \quad (4.7)$$

Although the above equations allow for a component of velocity in the z-direction, only in-plane motion is utilized in the simulation. Figure 4.3 provides overhead and side views of the orbital plane.

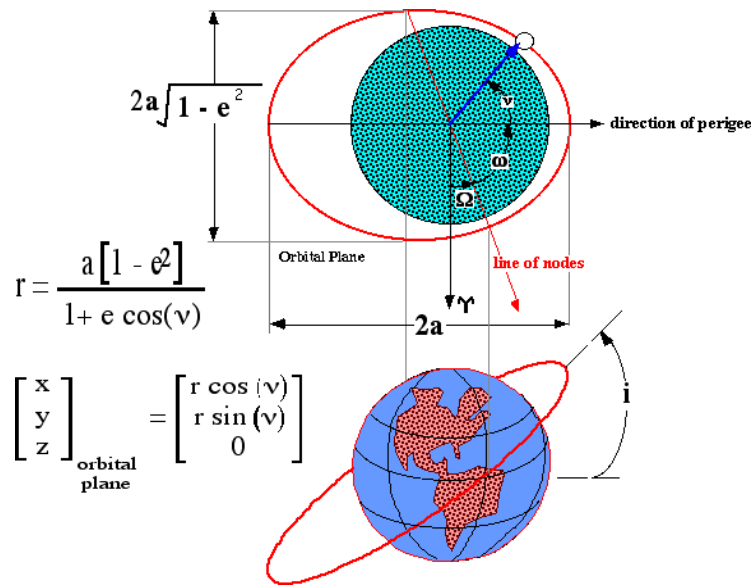


Figure 4.3 Polar/Planar Views of the Orbital Plane

C. DYNAMIC EQUATIONS USED BY SIMULATION

1. Orbital Energy

In an ideal Keplerian world, the specific orbital energy, \mathbf{e} , is constant.

$$\mathbf{e}_{orbit} = -\frac{\mathbf{m}}{2a_{orbit}} \quad (4.8)$$

If a non-conservative force is performing work on the vehicle operating in the orbit “a”, after a period of time t , the new orbital energy level is

$$[\mathbf{e}_{orbit}]_t = -\frac{\mathbf{m}}{(2a_{orbit})_t} = -\frac{\mathbf{m}}{(2a_{orbit})_0} + \frac{Energy\ change}{m_{vehicle}} \quad (4.9)$$

With this in mind, Kepler’s Laws no longer apply, and Newton’s Laws must be used to describe these orbits:

$$\text{Velocity} \quad \vec{V} = \frac{\partial \vec{R}}{\partial t} + \vec{\omega} \times \vec{R} \quad (4.10)$$

$$\text{Acceleration} \quad \frac{\sum \vec{F}_{external}}{M} = \frac{\partial \vec{V}}{\partial t} + \vec{\omega} \times \vec{V} \quad (4.11)$$

$$\text{Mass-change} \quad \dot{M}_{vehicle} = -\frac{F_{thrust}}{g_o \cdot I_{sp}} \quad (4.12)$$

2. Acceleration Vector

Since the coordinate system is moving with the orbiting spacecraft, the effects of the angular motion of the spacecraft must be accounted for. Therefore, the inertial rate of change of the vehicle’s velocity vector is given by the vector \vec{A} , where

$$\vec{A} = \begin{bmatrix} \dot{V}_r \\ \dot{V}_n \\ 0 \end{bmatrix} + \begin{bmatrix} \frac{-V_n^2}{r} \\ \frac{V_n V_r}{r} \\ 0 \end{bmatrix} \quad (4.13)$$

[Friedberger]. Newton's Second Law gives an expression for the force acting upon an object as the object's mass multiplied by the objects acceleration, or

$$\vec{F} = m \cdot \vec{A} \quad (4.14)$$

After some rearrangement of terms, it can be seen that the change in the vehicle's velocity is given by the expression

$$\begin{bmatrix} \dot{V}_r \\ \dot{V}_n \end{bmatrix} = \frac{\vec{F}}{m} - \begin{bmatrix} -\frac{V_n^2}{r} \\ \frac{V_n V_r}{r} \end{bmatrix} \quad (4.15)$$

3. Resolution of Forces

The force acting upon the launch vehicle can be broken down into four broad categories: gravity, thrust, and aerodynamic forces. As with the acceleration vector, each of these forces has a component in the radial (r) direction, and the tangential (n) direction.

a. Gravity

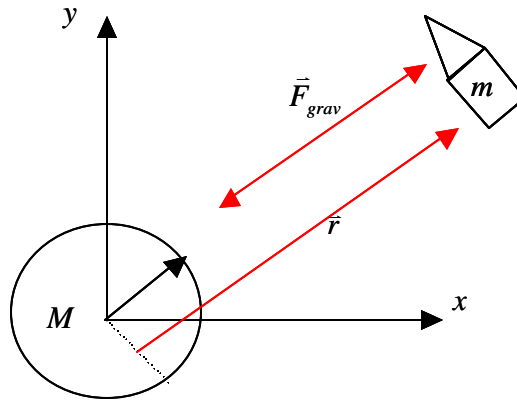


Figure 4.4 Gravity Force Diagram

The force of gravity is a conservative force. That is to say that it neither removes, nor adds energy to the orbit. Gravity is subject by the “inverse-square” law,

which states that the force varies as a function of $\frac{1}{|r|^2}$, and is represented by

$$\frac{\bar{F}_{grav}}{m} = \begin{bmatrix} -\frac{m}{|r|^2} \\ 0 \end{bmatrix} \quad (4.16)$$

b. Thrust

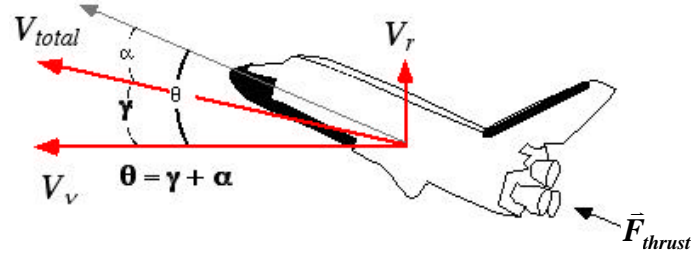


Figure 4.5 Thrust Force Diagram

Thrust is a non-conservative force that adds or removes energy from an orbit. A simplifying assumption is that thrust always acts along the direction of the longitudinal axis of the vehicle. The force due to vehicle thrust is given by the equation 4.17.

$$\frac{\bar{F}_{thrust}}{m} = \begin{bmatrix} \left[\frac{F_{thrust}}{m} \right]_r \\ \left[\frac{F_{thrust}}{m} \right]_n \end{bmatrix} = \begin{bmatrix} \frac{F_{thrust}}{m} \sin(q) \\ \frac{F_{thrust}}{m} \cos(q) \end{bmatrix} \quad (4.17)$$

c. Aerodynamic Forces

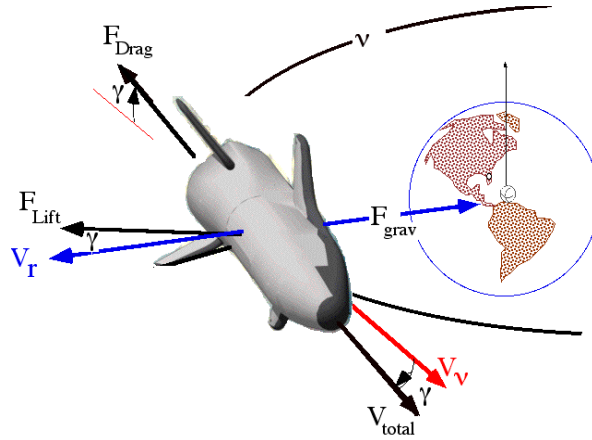


Figure 4.6 Vector Force Diagram

The aerodynamic forces, lift and drag, are non-conservative forces that remove or add energy to the vehicle's orbit. The lift force acts perpendicular to the total velocity vector, and the drag force opposes the total velocity vector. The aerodynamic forces are

$$\begin{bmatrix} F_r \\ F_n \end{bmatrix}_{aero} = \begin{bmatrix} Lift \cdot \cos(\mathbf{g}) - Drag \cdot \sin(\mathbf{g}) \\ -Drag \cdot \cos(\mathbf{g}) - Lift \cdot \sin(\mathbf{g}) \end{bmatrix} \quad (4.18)$$

where \mathbf{g} = flight path angle

This expression can in turn be rewritten in terms of the total velocity vector

$$\begin{bmatrix} F_r \\ F_n \end{bmatrix}_{aero} = \begin{bmatrix} \frac{V_n Lift - V_r Drag}{\sqrt{V_r^2 + V_n^2}} \\ -\frac{[V_n Drag + V_r Lift]}{\sqrt{V_r^2 + V_n^2}} \end{bmatrix} \quad (4.19)$$

d. Vehicle Mass

The rate of change in the vehicle's mass over time is given as

$$\dot{m}_{vehicle} = -\frac{F_{thrust}}{g_o \cdot I_{sp}} \quad (4.20)$$

The total mass of the vehicle at any point in time can be found by integrating the rate change over the interval of time and deducting this from the vehicle's initial mass

$$M_t = M_0 - \int_0^t \frac{F_{thrust}}{g_o \cdot I_{sp}} \quad (4.21)$$

4. Generalized Equations of Motion

It is now possible to describe the generalized equations of motion as a collection of the individual calculations previously performed

$$\begin{bmatrix} \dot{V}_r \\ \dot{V}_n \\ \frac{\partial}{\partial t}(h) \\ \dot{r} \\ \dot{\mathbf{n}} \\ \dot{m} \end{bmatrix} = \begin{bmatrix} \frac{V_n^2}{r} - \frac{\mathbf{m}}{|\mathbf{r}|^2} + \frac{F_{thrust}}{m} \cdot \sin(\mathbf{q}) + \frac{Lift \cdot \cos(\mathbf{g}) \cdot \cos(\mathbf{f}) - Drag \cdot \sin(\mathbf{g})}{m} \\ -\frac{V_n \cdot V_r}{r} + \frac{F_{thrust}}{m} \cdot \cos(\mathbf{q}) - \frac{[Drag \cdot \cos(\mathbf{g}) + Lift \cdot \sin(\mathbf{g}) \cdot \cos(\mathbf{f})]}{m} \\ -\frac{Lift \cdot \sin(\mathbf{f})}{m \cdot V_n} \\ V_r \\ V_n \\ r \\ -\frac{F_{thrust}}{g_0 \cdot I_{sp}} \end{bmatrix} \quad (4.22)$$

D. TRANSFORMATION FROM GAUSSIAN TO INERTIAL COORDINATE SYSTEMS

Because of significant non-conservative external forces (i.e. lift, drag, thrust) will be acting on the spacecraft, the instantaneous orbit will no longer remain constant. Thus the instantaneous orbit must be computed from the Gaussian on in-plane velocity and position vectors. The set of six classic orbital elements (COE) used to describe the instantaneous orbit with respect to the inertial coordinate system are

a – Semi-major Axis
e – Eccentricity
i – Inclination
Ω – Right Ascension of the Ascending Node
w – Argument of Perigee
n – True Anomaly

Figure 4.7 Classic Orbital Elements

These orbital parameters, and the inertial coordinate system, are depicted in Figure 4.8. Appendix C presents the transformations that allow the reader to compute the orbital parameters from the inertial velocity and position vectors.

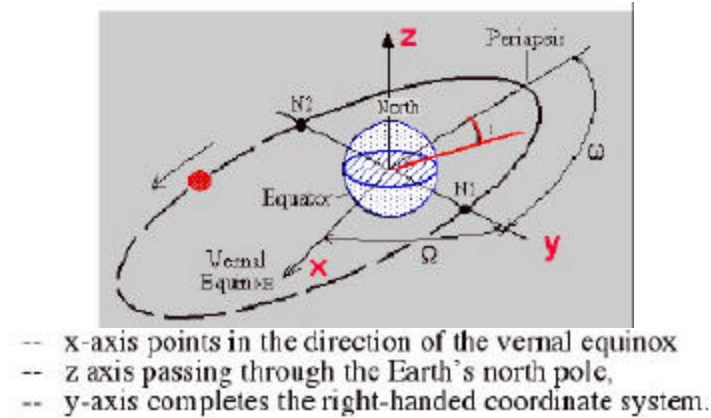


Figure 4.8 COE/Inertial Coordinate System

E. ATMOSPHERIC MODEL

The effects of lift and drag on the vehicle will be greatly dependent upon the vehicle's position within the Earth's atmosphere. For this analysis the 1976 standard atmosphere was used [NOAA].

Because the Earth's atmosphere is rotating with respect to the inertial coordinate frame, the rotation must be accounted for in order to obtain high accuracy in the lift and drag calculations. With respect to the inertial coordinate system, the rotational velocity of the atmosphere is expressed as the inner product of the inertial position vector, and the angular velocity of the Earth. This computed velocity vector due to Earth-rotation was then subtracted from the inertial velocity vector to give an estimate of the "wind-relative" velocity vector of the vehicle.

F. DEVELOPMENT OF AERODYNAMIC DATA

1. Software Programs

Several software programs were utilized in the development of the tools required during the course of this thesis research. AeroCFD and HyperCFD from Apogee Components provided the means of creating aerodynamic rocket forms and generating the accompanying aerodynamic data. Microsoft Excel was used to compile the aero data into spreadsheet form, and was instrumental in the validation of the AeroCFD/HyperCFD data.

a. AeroCFD

AeroCFD is a program that evaluates the aerodynamic qualities of a rocket design. The user is able to create original vehicle designs, or select from several stock rocket designs. From these designs, aero data can be generated for varying subsonic airspeeds and angles of attack (AOA). The AeroCFD user interface is depicted in Figure 4.9 below. The user is also able to select between compressible and non-compressible

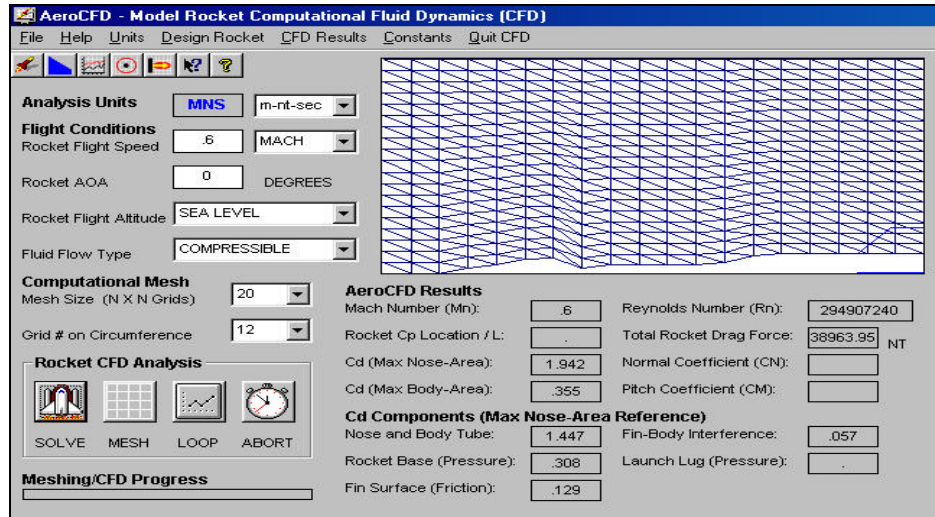


Figure 4.9 AeroCFD Front Panel Screenshot

fluid flow cases. AeroCFD uses the Prandtl-Glauert rule to estimate the effects of compressibility on air pressure and air velocity.

Once the aerodynamic data are generated for the rocket design, flow visualization can be accomplished. The user is provided with options for displaying velocity vector/contour plots, and static/dynamic pressure contour plots. Examples of the plots options are depicted in Figure 4.10.

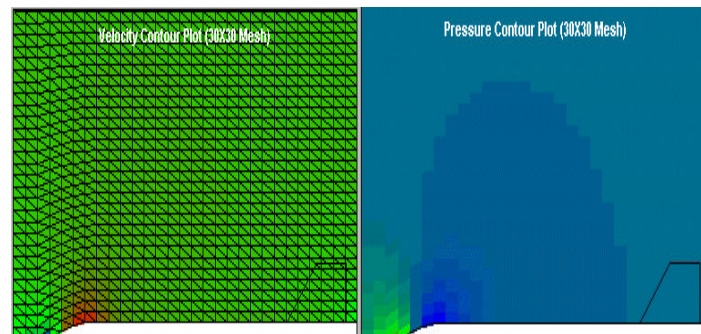


Figure 4.10 AeroCFD Plot Examples

b. HyperCFD

HyperCFD performs similar functions for flight regimes in the transonic region above Mach one. Once the vehicle design is finalized, aerodynamic data can be obtained for speeds greater than Mach 1.05. The US Standard Atmospheric Data (1962) is used for variation of pressure/density with changing altitude. Figure 4.11 depicts the HyperCFD front panel. HyperCFD makes use of the hypersonic similarity law to approximate the pressure coefficient (C_p) slightly above the transonic region ($M > 1.05$) [Hamaker]. Experimental pressure distribution results support this modification over a wide range of Mach numbers. A visual depiction of these results is given in Figure 4.12.

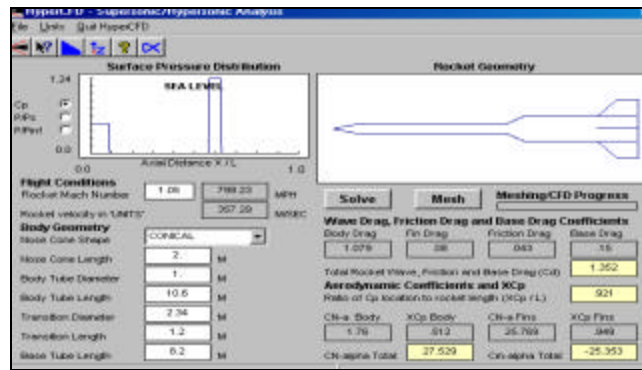


Figure 4.11 Hyper CFD Front Panel

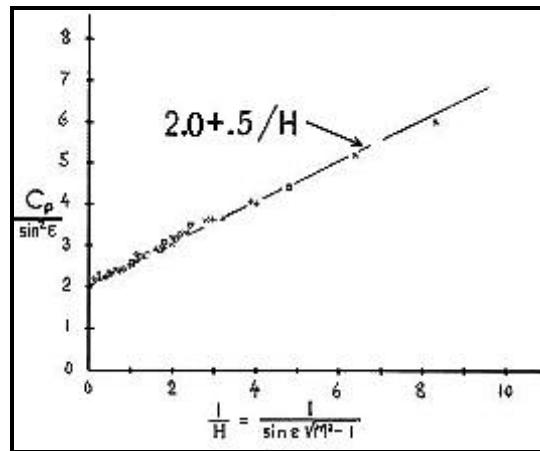


Figure 4.12 Hypersonic Similarity Approximations

2. Aerodynamic databases

Figure 4.13 depicts the individual stages and combined configuration for the notional launch vehicle. An axis-symmetric scramjet design was incorporated into the

second stage of the vehicle. This choice was made in an effort to avoid some of the problems associated with an asymmetric body-integrated design. The axis-symmetric design is easier to integrate into the launch stack, provides better heat dissipation (more uniform surface) than the body-integrated design, and most importantly is far more aerodynamically stable than an asymmetric design.

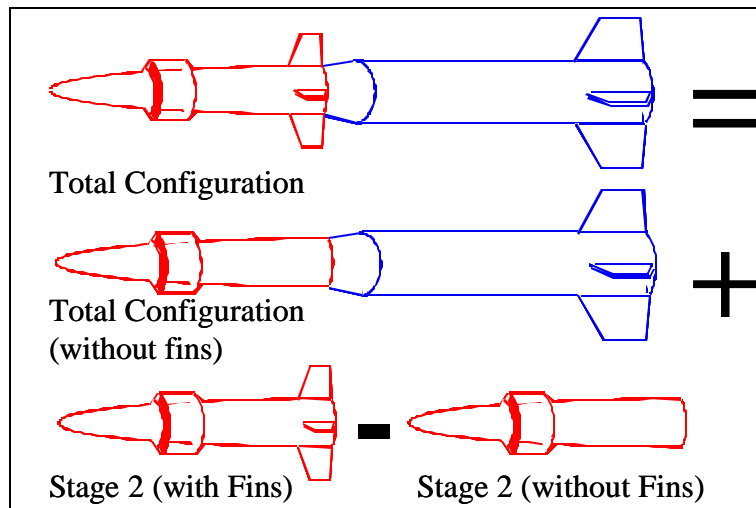


Figure 4.13 Notional Launch Vehicle Design

In order to determine the feasibility of SCRAMJET technology for an intermediate propulsive stage of an expendable launch vehicle, it was necessary to generate subsonic ($M < 1$) and supersonic ($M > 1$) aerodynamic data. These data were developed using AeroCFD for the subsonic case, and HyperCFD for the supersonic case. C_N and C_D are based upon the nose area of the vehicle. The calculations were repeated for each Mach and alpha. Units of meters, Newtons, and seconds (m-nt-sec) were carried throughout both programs.

a. Subsonic Data

The first step in obtaining the subsonic data was to define the body tube geometry of the notional launch vehicle. The program allows the user to select standard tube geometry or a free-form option. Figure 4.14 depicts the user interface. The user selects the basic nose cone shape from a pull-down menu and inputs dimension of the nose cone length, diameter and body tube length. The next step is to establish the number and configuration of fins (Figure 4.15) on the vehicle. Once the design of the vehicle is

completed, a solution for the complex fluid-flow is determined. The user then has the option of plotting these results, or modifying the vehicle geometry prior to resolving.

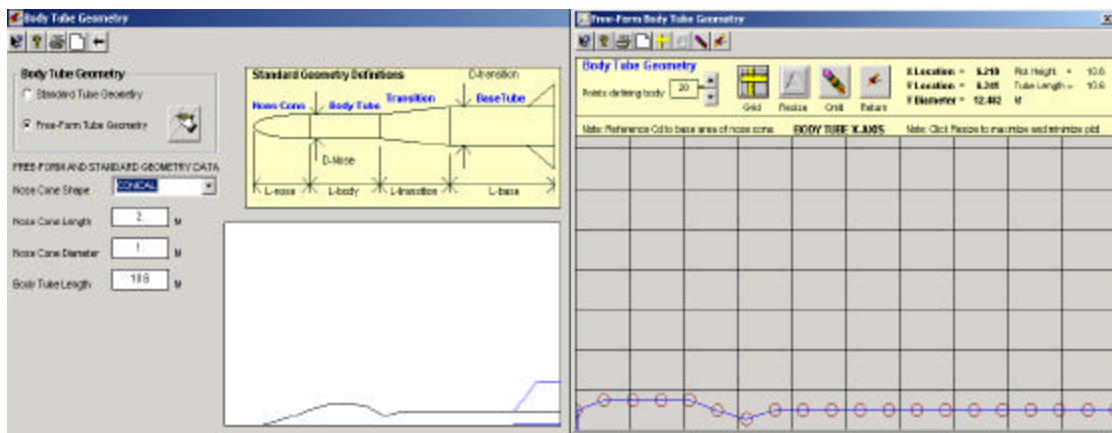


Figure 4.14 Body Tube Design

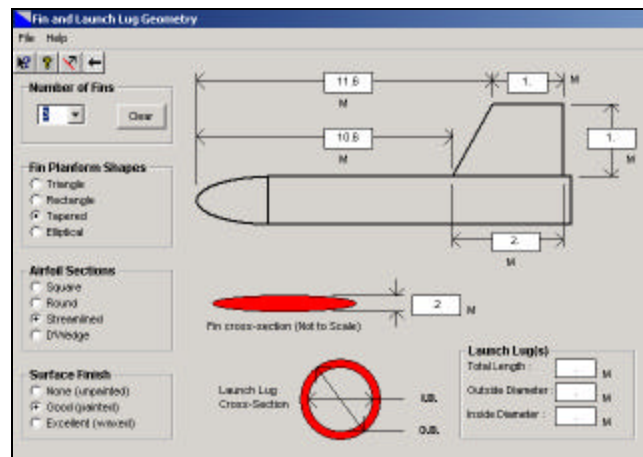


Figure 4.15 Fin Design

For designing the notional SCRAMJET launch vehicle, the free-form option was chosen. A conical nose cone shape was selected to approximate the inlet design of the SCRAMJET engine.

Flow solutions were computed for three components of the launch vehicle: launch configuration, stage II (with fins), and stage II (w/o fins). The later two designs were necessary to overcome the limitation of AeroCFD not allowing for multiple stage designs. The fins/sans fins designs were used to determine the “delta” correction that had to be added to the launch configuration CFD results. Data were obtained for angles of attack (AoA) of 0, 1, 2, 3, 5, 8, 10, and 15 degrees and velocities of 0, .2, .5, .7, and .8

Mach. Figure 4.16 depicts the launch configuration Cn/Cd subsonic data. Figure 4.17 depicts the Stage II (scramjet) Cn/Cd subsonic data. The tabular data are contained in Appendix B (Aerodynamic Databases).

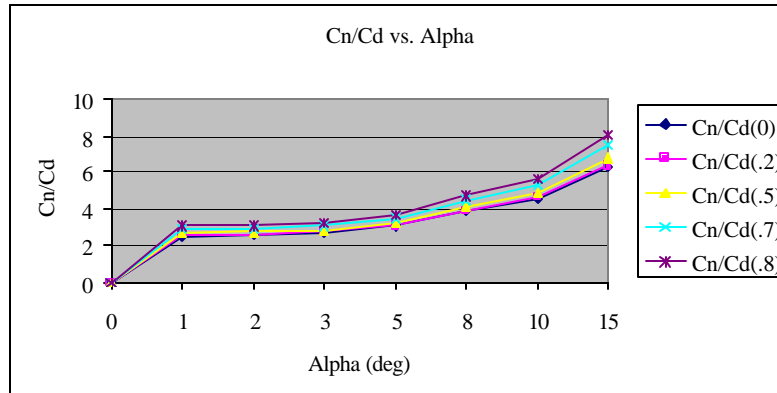


Figure 4.16 Launch Configuration Subsonic Data Plot

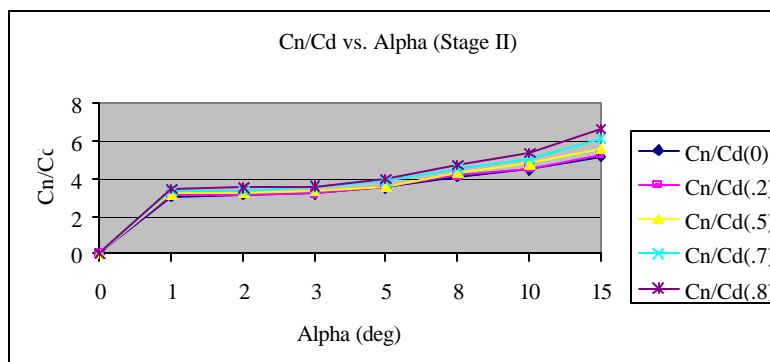


Figure 4.17 Stage II Subsonic Data Plot

b. Supersonic Data

HyperCFD was used to develop the supersonic aerodynamic data for the design. It was necessary to first establish the body geometry, then fin layout in a process similar to that used with AeroCFD. The interface is depicted in Figure 4.18.

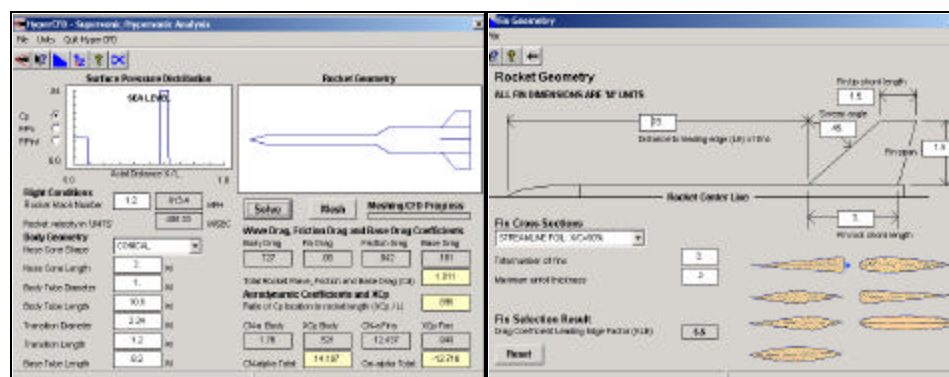


Figure 4.18 HyperCFD Body/Fin Design

Although both programs are developed by Apogee Components, the model developed for one was not transferable to the other. The same overall dimensions were used for the supersonic model as for the subsonic case. Minor differences in the body shape between the two designs were assumed to be negligible. Data were obtained for angles of attack (AoA) of 0, 1, 2, 5, and 8 degrees and velocities of 1.2, 1.5, 2, 5, 8, and 10 Mach. Figure 4.19 depicts the launch configuration Cn/Cd supersonic data. Figure 4.20 depicts the Stage II (scramjet) Cn/Cd supersonic data. The tabular data can be found in Appendix B (Aerodynamic Databases).

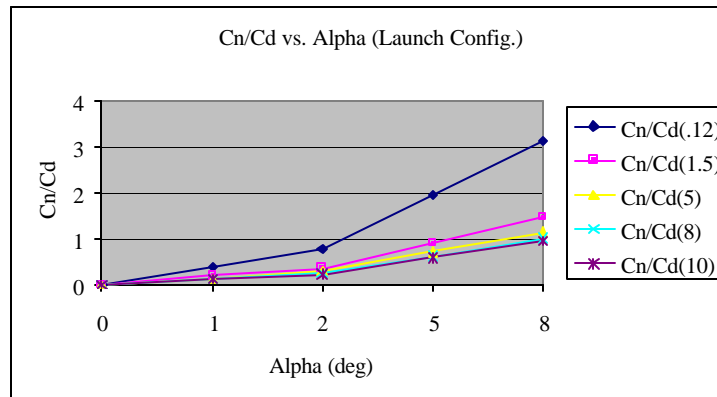


Figure 4.19 Launch Configuration Supersonic Data Plot

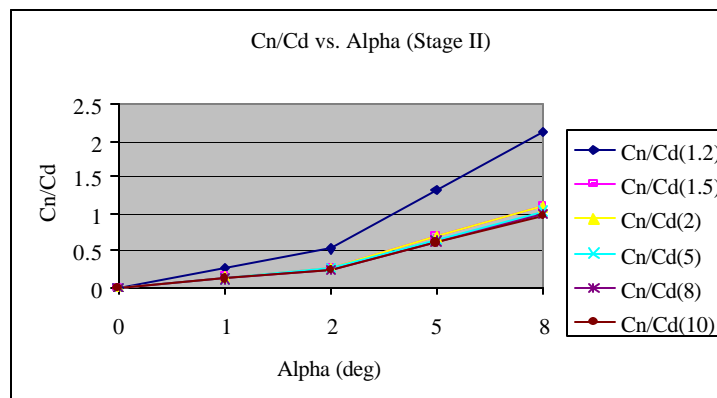


Figure 4.20 Stage II Supersonic Data Plot

G. LABVIEW

The simulation serves to provide insight as to which parameters are important to the problem. Batch simulations programmed using LabVIEW are capable of performing extended Monte-Carlo analyses. The "piloted" simulation tool can be used for generating feasible starting trajectories for subsequent optimization codes, such as POST and DIDO [Fahroo].

National Instruments LabVIEW (Laboratory Virtual Instrument Engineering Workbench) is a computer-based development environment leveraged upon graphical programming. LabVIEW makes use of graphical symbology to describe individual programming steps. The program's ease of use is largely due to its use of familiar scientific terminology, symbols, and ideas. LabVIEW supports communication with typical laboratory hardware, and plug-in data acquisition boards. The software comes with a tutorial complete with a glossary of terms, learning activities, and support resources.

Programs created in LabVIEW are referred to as Virtual Instruments (VIs). A VI makes use of functions to manipulate data from a variety of sources and display the results for the user. Each VI consists of three basic components: the Front Panel, the Block Diagram, and the Icon/Connector Pane.

1. Front Panel

The front panel is the user interface to the virtual instrument (VI). The panel is built using controls and indicators the user selects from the Control Palette. Controls serve as inputs to the block diagram of the VI. Indicators display the results of calculations, and can be used for intermediate check-cases for complex computations. Figure 4.21 shows the relationship of the Control Palette to the VI front panel.

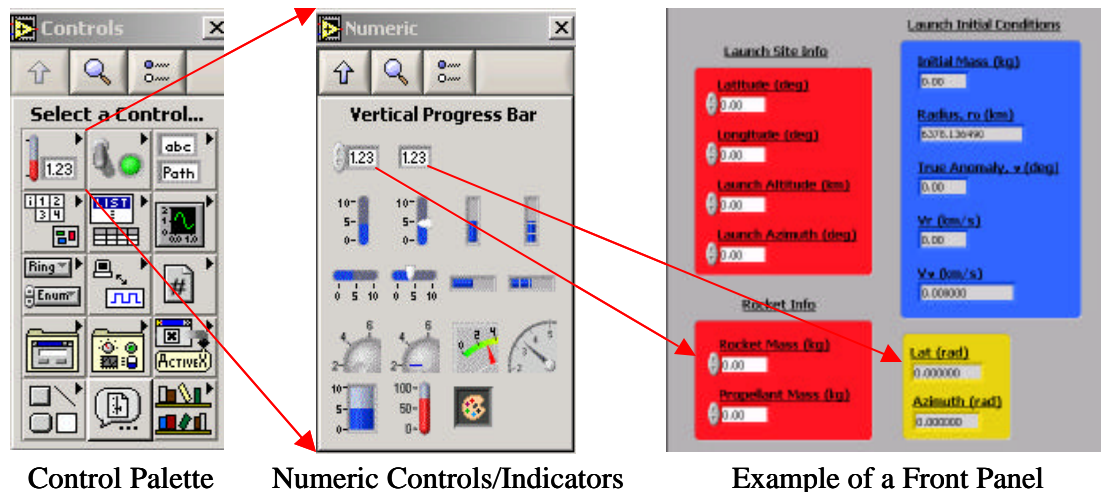



Figure 4.21 Control Palette/Front Panel

2. Block Diagram

The block diagram contains the graphical source code for the VI, and consists of terminals, functions, and wiring. Every item on the Front Panel appears as a terminal (i.e. ). Terminals take on the data type of the Control or Indicator that they represent. Terminals serve as access ports that allow the transfer of information between Front Panel items and the Block Diagram. For clarity of understanding, several terminals may be bundled together into clusters. User defined inputs are manipulated by functions within the Block Diagram, and the results of these calculations are returned to Indicators on the Front Panel. Wires represent the connections between Block Diagram items. Figure 4.22 shows the Block Diagram corresponding to the previous example VI.

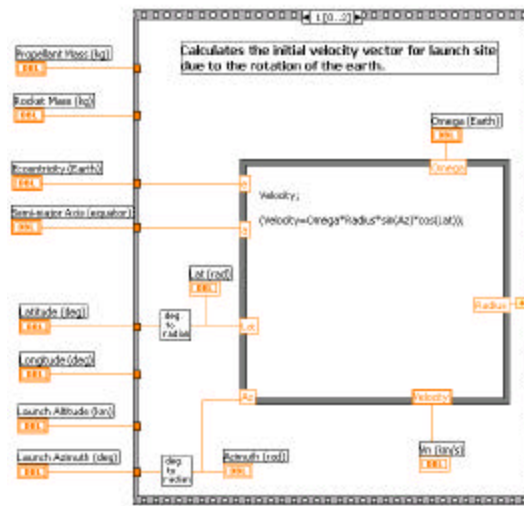



Figure 4.22 Example Block Diagram

3. Icon/Connector Panel

Once the Virtual Instrument is created, the Icon () serves as the graphical representation of the VI. The Icon can be edited so as to provide an obvious explanation of its function. This is extremely useful when embedding VIs within other Virtual Instruments.

The Connector Pane is the interface between the sub-VI and the Controls and Indicators located on the calling VI's Front Panel. The Connector Pane shows what type of inputs and outputs need to be wired to the terminals in order for the VI to function. Figure 4.23 provides a representation of terminal wiring for the example VI.

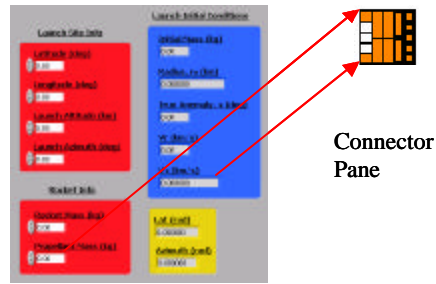


Figure 4.23 Example of Connector Pane Wiring

H. DEVELOPMENT OF SIMULATION TOOL

In order to create the launch simulation, it was first necessary to create various ancillary VIs that would be needed. Some of these instruments were used off-line from the actual simulation, providing a means of testing new ideas before changing the main body of code. A modular design philosophy allowed for a significant reuse of previously designed coding. The virtual instruments created can be categorized as performing one of three functions: data input/output, data manipulation, and presentation of results. While it would be tedious and excessive to cover every function-call of every VI, stepping through the calls made by the *Launch_Sim_Autopilot.vi* will provide a greater understanding of the components that comprise this main analysis tool. The overall process flow is depicted in Figure 4.24.

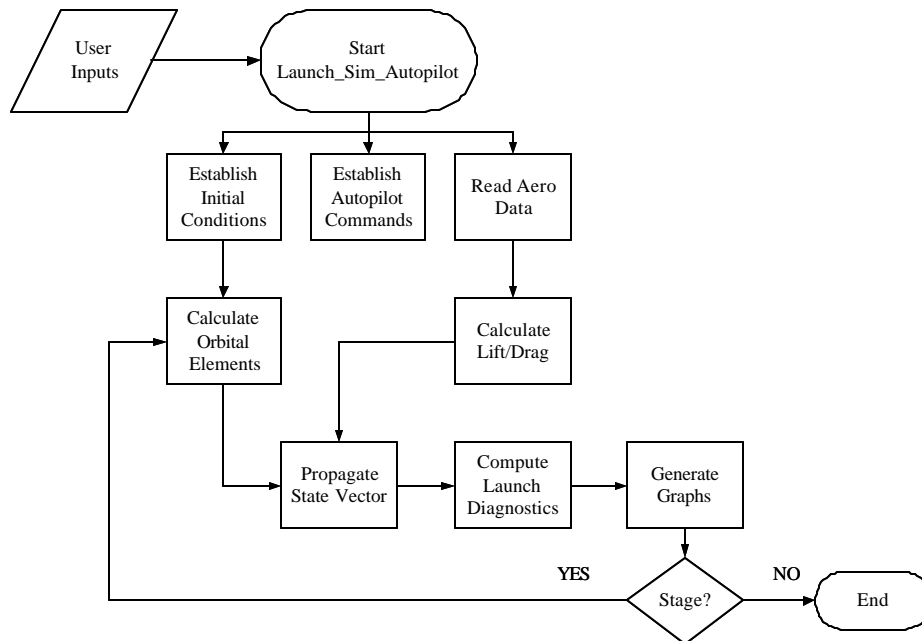


Figure 4.24 Process Flow Diagram

1. Front Panel Clusters

Launch_Sim_Autopilot.vi brings together data collected and the results of analyses performed offline by other VIs. The goal was to provide an analysis tool that the user can use to determine the performance and trajectory options for any launch-stack configuration. For ease of use, the Front Panel is divided into four functional areas or clusters: Setup, Autopilot/Waypoint Control, Dynamic Controls/Indications, and Orbital Plots.

a. Setup Cluster

The Setup cluster, depicted in Figure 4.25, brings together the aerodynamic model, vehicle propulsion data, and launch site and initial trajectory information. Based on this information, the resultant initial conditions are determined. The user is able to select the method of integration used. A launch diagnostics module is included in order to help determine the changes in velocity (ΔV) that are needed in order to improve the vehicle's ability to attain orbit compared to past simulation runs.

b. Autopilot/Waypoint Cluster

The Autopilot/Waypoint Control cluster (Figure 4.26) allows the user to define initial values, weights, and auxiliary outputs for the automatic pitch and throttle controls. Additional inputs are the initial and final pitch values, the target point for stage one burnout, the intermediate waypoints (based upon Mach) and the associated commanded pitch change. An XY-graph is included to visually depict pitch angle vs. time data. All of the inputs feed into the *Launch_Sim-Autopilot.vi* to enable the user to define trajectories in a much easier and intuitive fashion than is possible using current trajectory design programs such as POST.

The screenshot displays the front panel of the *Launch_Sim_Autopilot.vi* software, organized into several functional clusters:

- Launch Site Info:** Includes input fields for Latitude (deg) at 28.43, Longitude (deg) at -80.68, and Launch Altitude (km) at 0.00.
- Initial trajectory info:** Includes Launch Azimuth, γ (deg) at 90.00, Flight Path Angle, α (deg) at 90.000, and Airspeed, V_a (km/s) at 0.000.
- Default Aero data file path:** A text field showing the path *C:\Users\WJ\Archive2\June02\Aero\default_config_aero.txt*.
- Propulsion Stage data:** A table for Stage 1 with the following values:

Structural mass (kg)	Exit Velocity (m/sec)
1.5000E+4	4.8000E+3
Initial Propellant mass (kg)	Exit Pressure (Pa)
2.0000E+4	2.3940E+4
Payload mass (kg)	Exit Area (m ²)
5.8000E+3	1.3990E+3
Nominal Massflow (kg/sec)	Stage #
2.0000E+2	1
- Initial Conditions:** Includes V_e (km/s) at 1.000E28, V_0 (km/s) at 1.400E28, Inclination, i (deg) at 0.00, R (km) at 6375.284373, True Anomaly, θ (deg) at 180.00, and Mass (kg) at 200004.38.
- Integrator:** Radio buttons for Runge Kutta (selected) and Trapezoidal rule.
- Launch Diagnostics:** Includes Perigee Altitude (km) at -4420.61, Apogee Altitude (km) at 51.09, and Remaining Propellant Mass for stage at 5.69.

Figure 4.25 Setup Cluster

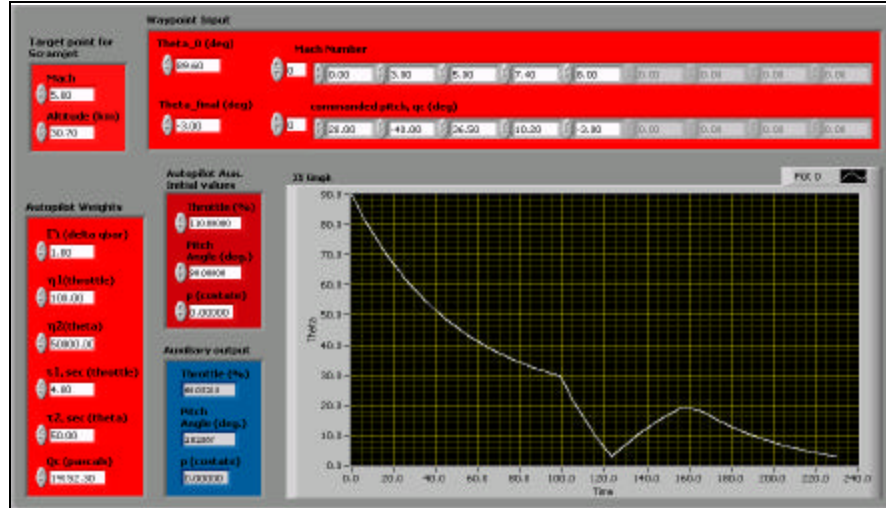


Figure 4.26 Autopilot/Waypoint Control Cluster

c. *Dynamic Controls/Indications Cluster*

The Dynamic Controls/Indications cluster (Figure 4.27) contains the pitch, roll, throttle, autopilot, and master run/stop controls. Indicators include the current state vector, external forces, instantaneous orbital and atmospheric trajectory elements, commanded pitch and throttle settings, and elapsed simulation time (in sec). Plots depict altitude vs. downrange, and altitude vs. Mach data of the resultant vehicle trajectory. Lines of constant q_{bar} are included in order to provide a visual reference to the ideal trajectory.

Figure 4.28 depicts the two different methods of displaying the orbital path within the Orbital Paths cluster. While its use is unimportant during the launch phase of operations, the vehicle position within the orbital plane is vital when executing post-launch orbital insertion maneuvers. The geocentric ground-trace aids launch planners in determining quickly whether a planned launch azimuth will come close to population centers. Together, these two visual depictions of position within the orbital plane provide quick, easily interpreted indications of the vehicle's current position, as well as its ability to attain orbit.

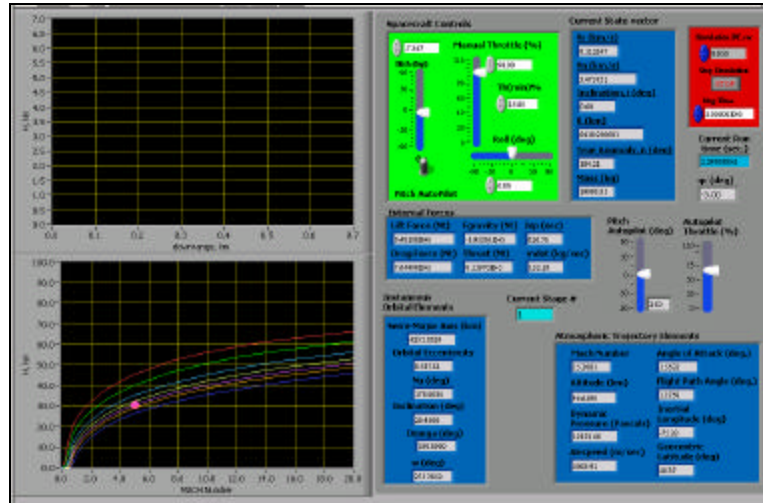


Figure 4.27 Dynamic Controls/Indications Cluster

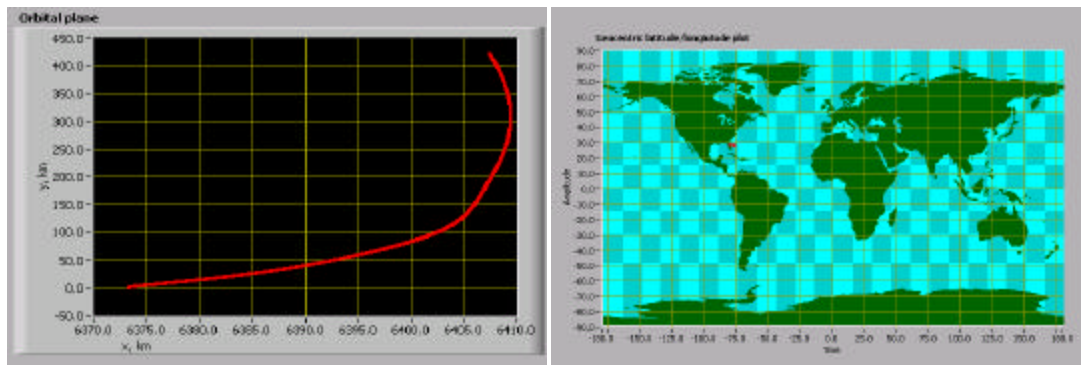


Figure 4.28 Orbital Plane/Geocentric Ground Trace

2. Order of Execution

When the Run button on the Front Panel of *Launch_Sim_Autopilot.vi* is activated, the contents of each frame are activated in succession. The first frame contains the *Initial_Conditions.vi*. This retrieves the launch site, initial trajectory, and propulsion stage data, and calculates the launch initial conditions; launch velocity components, and initial orbital elements. The VI Diagram is depicted in Figure 4.29. These data are in turn used to calculate the velocity boost at the launch site due to the rotation of the earth, as well as computing the initial x/y coordinates for plotting.

The second frame contains *Constant_qbar_lines.vi*. This VI takes the target point for SCRAMJET activation as input and plots the lines of constant q_{bar} as overlays on the altitude vs. Mach graph.

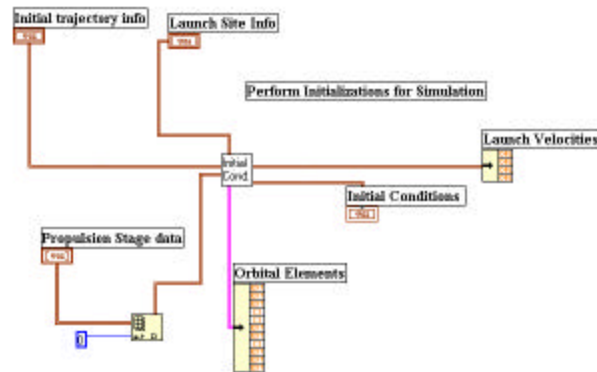


Figure 4.29 *Initial_Conditions.vi* Diagram

The third frame reads in the aerodynamic data using the VI called *Read_aero_data.vi*. This retrieves the aerodynamic data file that was created off-line using AeroCFD/HyperCFD. The data are retrieved from the file location and are manipulated into the output aero data array (Figure 4.30). This array serves as one of the inputs to the autopilot VI.

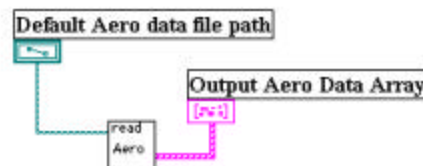


Figure 4.30 *Read_aero_data.vi*

The remaining sub-frames of the *Launch_Sim_Autopilot.vi* are dependent upon the previously collected data. Table 4.1 gives a quick snapshot of the functionality of each frame. Sub-frames 0, 1, 2, and 5 will be covered in more detail.

a. Sub-frame 0

Sub-frame 0 is where the autopilot calculations are performed. Figure 4.31 depicts the dataflow for the major features of the frame. *Autopilot.vi* receives input from the input clusters (Initial Conditions, Spacecraft Controls, Atmospheric Trajectory Elements, External Forces, Simulation Controls, and Autopilot Aux. Initial Values and Weights). A logical case structure contains a provision for utilizing waypoints during flight. Vehicle pitch can be commanded to target values occurring at discrete Mach

values. The VI then calculates the output clusters (auxiliary state vector, and autopilot controls), which serve as inputs for successive frames.

Sub-frame	Function
0[0..7]	Autopilot Calculations
1[0..7]	Propagate the State Vector
2[0..7]	Launch Diagnostics
3[0..7]	Plot S/C Posn. in Orbital Plane
4[0..7]	Plot Alt. vs. Downrange
5[0..7]	Manage S/C Mass
6[0..7]	Plot Geocentric Lat./Long.
7[0..7]	Plot Alt. vs. Mach

Table 4.1 VI Frame Functions

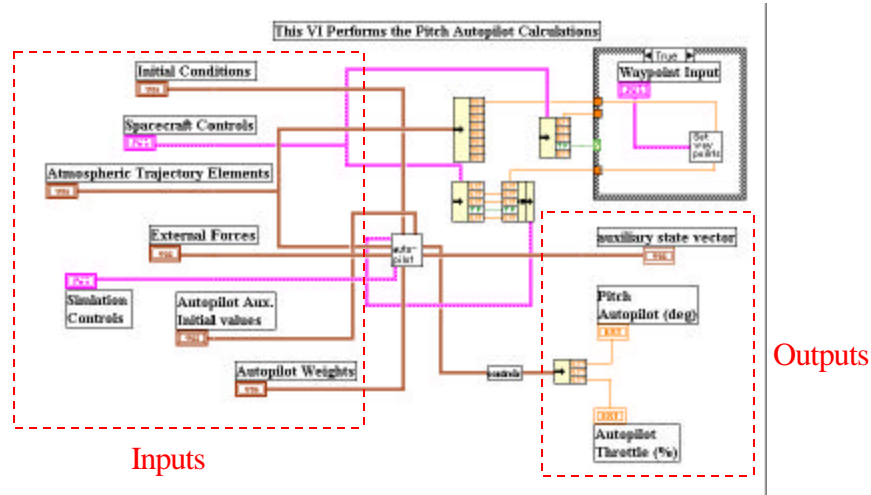


Figure 4.31 Sub-frame 0 (Autopilot Calculations)

Figure 4.32 depicts the data-flow for the state vector propagator. The user selects between Runge-Kutta and Trapezoidal rule for the method of integration to be used. When Runge-Kutta is selected, the propagator predicts the values of k_1, k_2, k_3, k_4 in order to determine the fourth-order state vector:

$$\hat{X}_{k+1} = \hat{X}_k + \frac{\Delta t}{6} [k_1 + 2k_2 + 2k_3 + k_4] \quad (4.23)$$

The Trapezoidal Rule first predicts the state vector using explicit Euler Integrations,

$$\widehat{X}_{k+1} = X_k + \Delta t \cdot \dot{X}_k(X_k) \quad (4.24)$$

then corrects the state vector:

$$X_{k+1} = X_k + \frac{\Delta t}{2} \left[\dot{X}_k(X_k) + \dot{\widehat{X}}_{k+1}(\widehat{X}_{k+1}) \right] \quad (4.25)$$

The selected propagator VI receives input from Initial Conditions, Autopilot Controls, Propulsion Stage Data, Aero Data, as well as selected values from Initial Orbital Elements (Ω , i , ω), and Simulation Controls (simulation time-step).

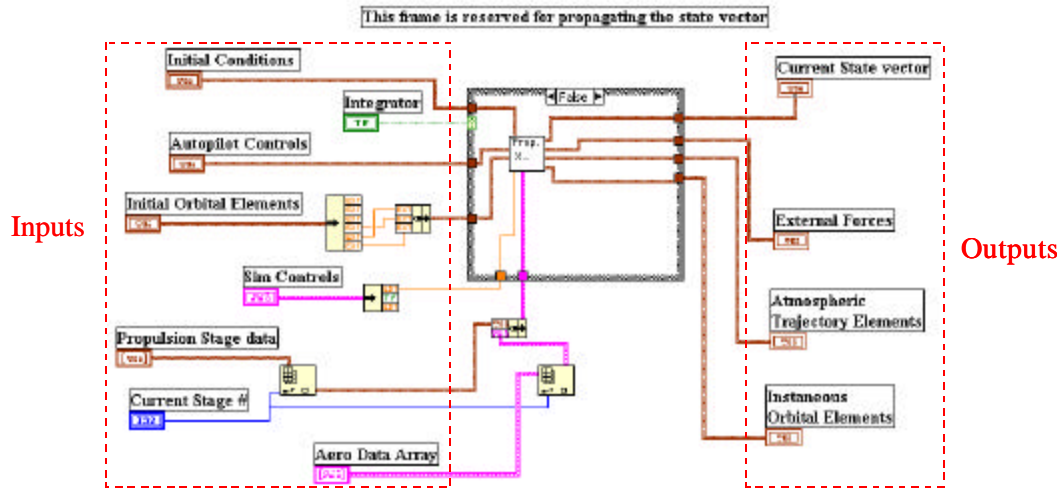


Figure 4.32 Sub-frame 1 (Propagate State Vector)

Embedded within each propagator VI, is *forces_xdot.vi*. This VI performs the orbital and atmospheric calculations, calculates the altitude variable thrust and mass-flow, computes the gravitational force, aerodynamic force coefficients and Lift/Drag forces, and \dot{X} . A complete derivation of the equations necessary for transforming from the perifocal to the inertial plane, deriving the orbital elements, and establishing the initial conditions is provided in Appendix A.

b. Sub-frame 2

Sub-frame 2 (Launch Diagnostics), depicted in Figure 4.33, performs launch diagnostics. It computes perigee and apogee altitudes and remaining propellant

mass. This provides the user with an instantaneous view of key parameters, with which they will be better able to determine the launch vehicle's ability to achieve orbit.

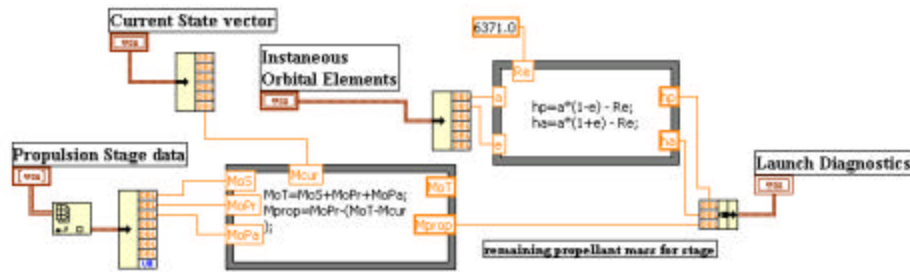


Figure 4.33 Sub-frame 2(Launch Diagnostics)

c. Sub-frame 5

Sub-frame 5 (Manage S/C Mass), depicted in Figure 4.34, manages the launch vehicle's mass during the staging process. The Launch Diagnostics cluster is tied to a Boolean case structure. Remaining propellant mass is compared to the null case (depleted fuel). If the value of remaining fuel is ≤ 0 , then stage burnout has occurred, the current stage # is incremented by one, and the user is queried whether or not to ignite the following stage. If the remaining fuel is ≥ 0 , the stage is still producing thrust, and the current stage vector is propagated out. Next, a logical AND operation is performed,

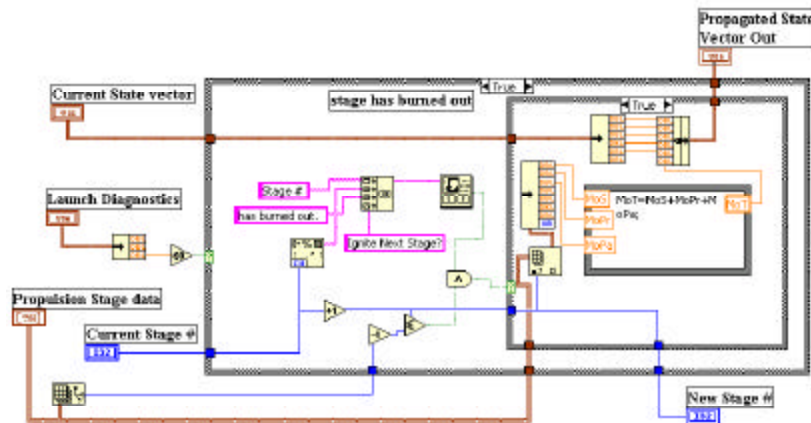


Figure 4.34 Sub-frame 5(Manage S/C Mass)

which compares the logical value of the user's decision and whether remaining vehicle stages exist. A result of TRUE updates the propagated state vector. A result of FALSE displays a message (Figure 4.35) stating the vehicle failed to achieve orbit.

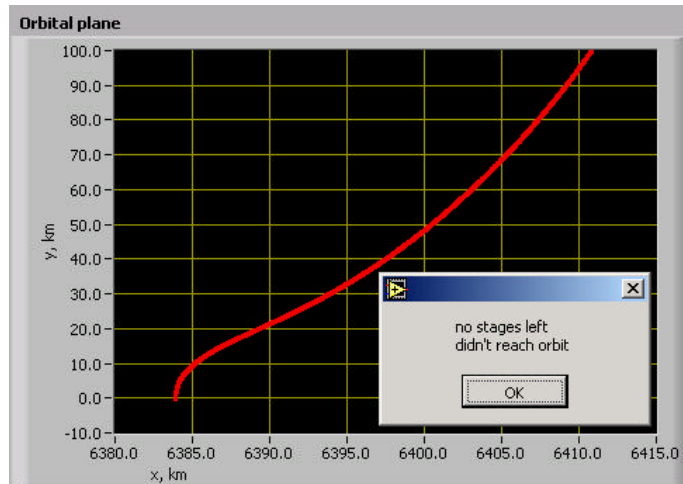


Figure 4.35 User Dialog Box

3. Using Launch_sim_autopilot

A real-world example was chosen to illustrate the operation of *Launch_Sim_Autopilot.vi*. NASA's hypersonic X-43A test vehicle was selected for several reasons. First, the X-43 represents the most developed US hypersonic vehicle design. Technical specifications for the X-43 and its Orbital Science Corporation Pegasus booster were readily available in aerospace literature. Also, Dryden Flight Research Center had expressed an interest in using the simulations trajectory design feature to determine possible flight profiles for the future flights of the X-43B and X-43C variants. Both generic and Hyper-X specific aerodynamic models were utilized in validating the launch simulation. The results were very similar for each model.

The Reagan Test Site, Kwajalein Atoll was chosen as the launch point. The Pegasus launch system had previously operated from the site, and its location at 9° North latitude provides an increase in the “delta-V” of the launch vehicle of approximately 0.46 km/s when launched in the direction of earth rotation. An easterly launch trajectory was chosen for the Reagan Test Site.

a. *Pegasus Launch System*

Pegasus is a commercial launch system developed by the Orbital Sciences Corporation. The system consists of the air-launched Pegasus rocket, and its Orbital Carrier Aircraft (OCA), dubbed the “Stargazer,” which is a Lockheed L-1011 commercial transport aircraft modified to carry the air-launched Pegasus rocket. This arrangement provides for improved performance over conventionally launched vehicles

of the same size. It also enables the Pegasus to operate from any location with a suitable airfield. Launch costs are on the order of \$12-15 Million USD.

A specially modified first stage of the Pegasus XL was used in the launch stack configuration. The second stage of the configuration consisted of the X-43 test vehicle. The modified Pegasus first stage booster, with the X-43A craft mounted to its nose, was carried by NASA's B-52 jet (Figure 4.36).



Figure 4.36 X-43 Launch Configuration

Performance and mass information for the Pegasus 1st stage was taken from the International Reference Guide to Space Launch Systems [AIAA 3rd Ed.]. Similar information for the X-43 test vehicle was obtained from Dr. Stephen Whitmore, at NASA Dryden Flight Research Center [Whitmore]. The propulsion stage information for all stack components is depicted in Figure 4.37.

Pegasus XL		X-43	
Structural mass (kg)	Exit Velocity (m/sec)	Structural mass (kg)	Exit Velocity (m/sec)
2.8860E+3	2.7408E+3	1.0000E+3	4.0000E+3
Initial Propellant mass (kg)	Exit Pressure (Pa)	Initial Propellant mass (kg)	Exit Pressure (Pa)
1.5048E+4	1.21042E+4	3.6300E+2	2.39403E+4
Payload mass (kg)	Exit Area (M ²)	Payload mass (kg)	Exit Area (M ²)
1.3610E+3	2.2400E+0	1.0000E+1	1.1898E+1
Nominal Massflow (kg/sec)	Stage #	Nominal Massflow (kg/sec)	Stage #
2.0500E+2	1	2.0000E+2	2

Figure 4.37 Propulsion Stage Data

b. Launch Trajectory

An easterly launch trajectory was chosen for the Reagan Test Site (Figure 4.38). The Reagan Test Site encompasses approximately 750,000 square miles, although the total land area is only about 70 square miles. Its location at 9° North Latitude provides an increase in the “delta-V” of the launch vehicle of approximately 0.46 km/s when launched in the direction of earth rotation. Also, Orbital Sciences Corporation



Figure 4.38 Reagan Test Site

had previously conducted the launch of the High Energy Transient Experiment (HETE) II spacecraft from RTS on October 9, 2000 [Ray].

Geographic coordinates of 9.00°N, and 166.08°E were chosen for the launch point. Launch altitude was taken to be 6.32 km. Launch airspeed of 0.16 km/s, a launch azimuth of due east, and a flight-path angle of 2° were chosen as initial trajectory elements. Figure 4.39 depicts the Autopilot/Waypoint Control Cluster settings used for the RTS launch.

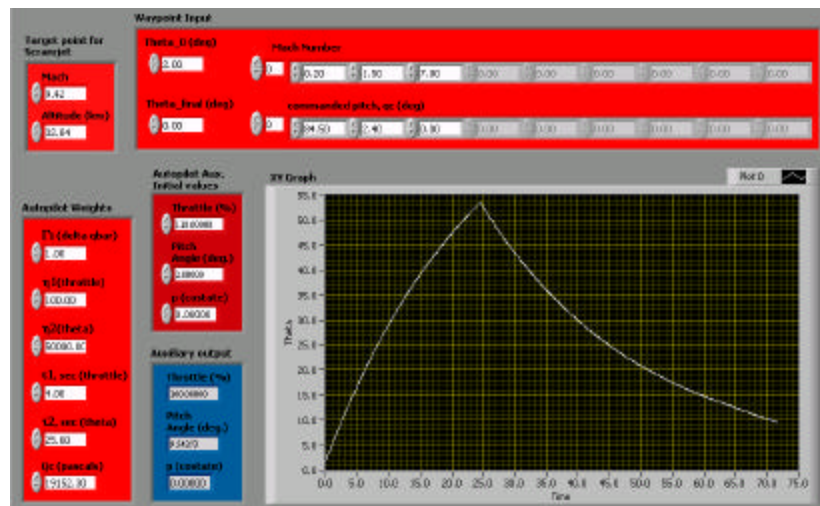


Figure 4.39 Autopilot/Waypoint Control Cluster

All inputs were fed into *Launch_Sim_Autopilot.VI*. The simulation was programmed to intercept the 1000 psf q_{bar} line after launch. With the autopilot engaged, stage one burnout occurred at an altitude of 32.6 km, at a velocity of Mach 9.43. The maximum cross loading of the vehicle was 106 psf. The plot of the trajectory from launch to stage one burnout is given in Figure 4.40.

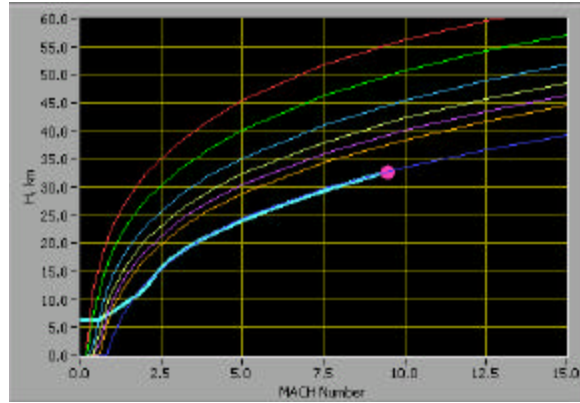


Figure 4.40 RTS Launch Trajectory (Default Aero)

Utilizing the X-43 specific aerodynamic data, stage one burnout occurred at an altitude of 37.9 km, at a velocity of Mach 10.3. The maximum cross loading of the vehicle was 374 psf. The plot of the trajectory from launch to stage one burnout is given in Figure 4.41.

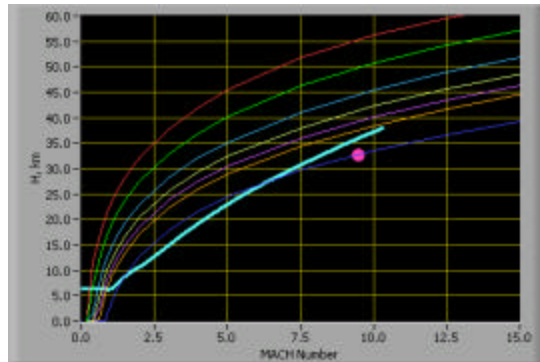


Figure 4.41 RTS Launch Trajectory (X-43 Aero)

THIS PAGE INTENTIONALLY LEFT BLANK

V. ANALYSIS CASE STUDY

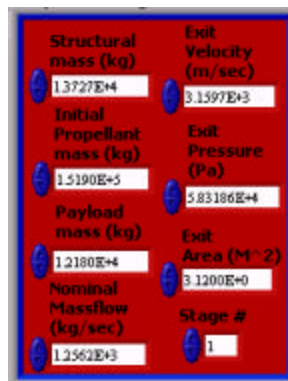
A. METHODOLOGY

In an effort to qualitatively show the potential performance benefits of including a scramjet within the launch vehicle stack, several case studies were conducted. A standard configuration Atlas III was chosen for the baseline expendable launch vehicle. A modified Atlas III, incorporating an axis-symmetric scramjet engine, was to illustrate the performance of a scramjet enabled design.

To address the possible economic benefits of incorporating scramjet technology, three cases were used. As in the performance section, the baseline Atlas III and scramjet enabled Atlas III launch vehicles, were considered. A third economic case was selected as well, wherein the Atlas III was assumed to be partially reusable.

B. INITIAL CONDITIONS

For the purpose of this analysis, all vehicles were assumed to launch from the geographic coordinates of 27.5° N Latitude, and 80.0° W Longitude. Launch azimuth was chosen as due east, in order to take advantage of the increase in “delta-V” due to launching in the direction of the earth’s rotation. Each vehicle design incorporates a “mission payload” (payload + structure + fuel) of 4000kg, which is to be delivered into orbit. Figure 5.1 depicts the propulsion stage characteristics of the Atlas III first stage that served as the backbone for each of the launch vehicle designs.



Structural mass (kg)	Exit Velocity (m/sec)
1.3727E+4	3.1597E+3
Initial Propellant mass (kg)	Exit Pressure (Pa)
1.5190E+5	5.8318E+4
Payload mass (kg)	Exit Area (M ²)
1.2180E+4	3.1200E+0
Nominal Massflow (kg/sec)	Stage #
1.2562E+3	1

Figure 5.1 Atlas III 1st Stage Characteristics

One of several important points to consider is that while both vehicles utilize the same first stage, there are constraints placed upon the scramjet-enabled design that the

Atlas III is not subject to. The Atlas III quickly climbs out of the atmosphere, whereas the Atlas III-SCRAM must follow along the 1000 psf pressure (q_{bar}) profile in order to ensure ignition of the scramjet. Also, the Atlas III is able to modulate throttle/pitch settings in order to arrive at the desired apogee altitude. The Atlas III-SCRAM must fly the prescribed profile until the fuel is expended. Once the apogee altitude is attained, a final boost is required to circularize the orbit.

C. ATLAS III

1. Configuration Data

The Atlas III vehicle (Figure 5.2) is an improved version of the established Atlas II family of launch vehicles. The 1st stage incorporates a single NPO Energomash RD-180 engine. Two versions of the Atlas III are currently available, with differences only in the number of engines in the Centaur stage.



Atlas III

Height:	28.91m
Diameter:	3.05m
Total Launch Mass:	177,807kg
Dry Mass:	19,907kg
Pmf:	7.93

Figure 5.2 Atlas III

The Atlas IIIA has a single RL-10A-4-2 engine powering the Centaur upper stage while the Atlas IIIB has two RL-10A-4-2 engines and a stretched Centaur upper stage to increase geosynchronous transfer orbit delivery performance to just under 10,000 lb. International Launch Services (ILS) is marketing both vehicles [[Atlas III](#)]. Figure 5.3 depicts the propulsion data for the upper stage.

Propulsion Stage data	
Structural mass (kg)	Exit Velocity (m/sec)
2.1800E+3	4.2435E+3
Initial Propellant mass (kg)	Exit Pressure (Pa)
3.2250E+3	0.0000E+0
Payload mass (kg)	Exit Area (M^2)
4.0000E+3	1.0700E+0
Nominal Massflow (kg/sec)	Stage #
2.2430E+2	2

Figure 5.3 Centaur Upper Stage

2. Trajectory Design

Initially, two different orbits were selected for designing the conventional Atlas III trajectories. The first was to a final low earth orbit (LEO) of 165km, and the second envisioned a re-supply mission to the International Space Station (ISS). Both utilized the autopilot designed into the launch simulation.

After initial analysis, it was found that the conventional Atlas III was unable to cost effectively achieve the LEO target. At stage 1 burnout, the Atlas III has already achieved an apogee altitude of 200km. Re-supplying the ISS was chosen as the baseline mission for analysis purposes. The space station maintains an orbit between 362-476km [ISS]. A target orbit of 425km was selected.

Figure 5.4 depicts the ISS service mission trajectory for the Atlas III. The target point for stage one burnout and waypoints used are depicted in Figure 5.5. For each chosen Mach break point, there is a corresponding commanded pitch angle (q_c). The autopilot initial values and weighting factors used in the trajectory design are shown in figure 5.6.

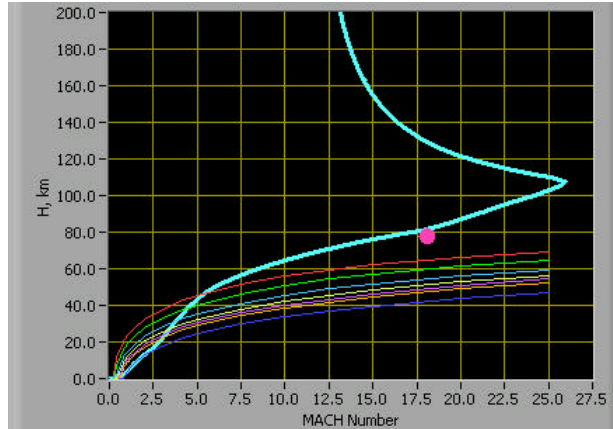


Figure 5.4 Atlas III ISS Service Trajectory

Figure 5.5 Autopilot Waypoint Values

Figure 5.6 Autopilot Weights/Initial Values

3. Highlights

The following section performs the mathematical portion of the analysis of the Atlas III performance. The amount of “delta-V” achieved is given at stage one and two burnout. Also, the final velocity change to circularize the final orbit is determined.

a. Stage 1 Burnout

Figure 5.7 depicts the altitude/velocity profile of the Atlas III at the time of stage one burnout. Stage one burnout occurs at an altitude of 81.0466km. At the time

of engine burnout, the Atlas III is traveling at Mach 17.879 (4.999km/s). The vehicle has traveled a downrange distance of more than 120km.

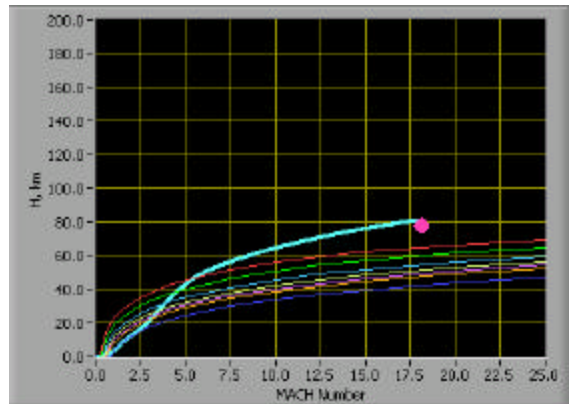


Figure 5.7 Atlas III Stage One Burnout

b. Stage 2 Burnout

Figure 5.8 depicts the altitude/velocity profile of the Atlas III at the time of stage two burnout. Stage two burns out at an altitude of 95.538km. At the time of engine burnout, the Atlas III is traveling at Mach 24.3619 (6.750km/s). The vehicle has traveled a total downrange distance just shy of 200km.

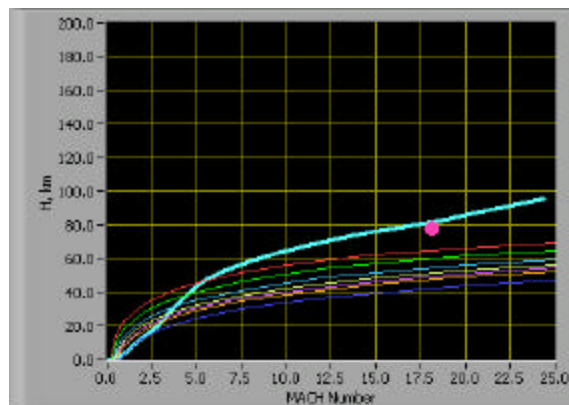


Figure 5.8 Atlas III Stage Two Burnout

c. Apogee Burn

Once the second stage burns out, the remaining mission payload enters a coast phase. Airspeed is traded for altitude until the payload reaches apogee (Figure 5.9). The final step is to determine the amount of “delta-V” that an apogee kick motor (AKM) would have to provide in order to circularize the orbit and keep the payload from reentering the earth’s atmosphere.

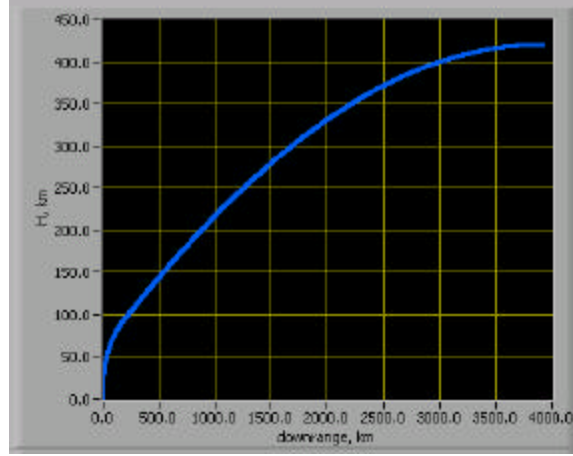


Figure 5.9 Atlas III Apogee Altitude

The velocity of the vehicle can be broken down into radial and tangential components,

$$V = \sqrt{\frac{m}{R}} \Rightarrow \vec{V} = \begin{pmatrix} V_r \\ V_n \end{pmatrix} \quad (5.1)$$

The change in velocity can then be expressed as:

$$\Delta \vec{V} = \begin{pmatrix} V_r \\ V_n - \sqrt{\frac{m}{R_{orbit}}} \end{pmatrix} \quad (5.2)$$

where: m = earth's gravitational parameter = $3.986 \times 10^5 \frac{km^3}{s^2}$

R_{orbit} = orbital radius = $6371.00 km + h$

Deriving an expression for the “delta-V” required for circularizing the final orbit results in:

$$\Delta V = \sqrt{V_r^2 + \left(V_n - \sqrt{\frac{m}{R_{orbit}}} \right)^2} \quad (5.3)$$

At apogee, $V_r \cong 0$, and $V_n = 6.735036 \frac{km}{s}$. Substituting numerical values into the above equation yields the following expression for the required “delta-V”:

$$\Delta V = \sqrt{0 + \left(6.735036 \frac{km}{s} - \sqrt{\frac{3.986 \times 10^5 \frac{km^3}{s^2}}{(6371 + 425.85) km}} \right)^2} = 0.9230 \frac{km}{s}$$

Now that we know the amount of “delta-V” necessary to circularize our final orbit, it remains to be determined what amount of fuel is require for this task. This takes us back to the now familiar rocket equation. In its simple form, the rocket equation is:

$$\Delta V = I_{sp} \cdot g_0 \cdot \ln \left(\frac{m_{initial}}{m_{final}} \right) \quad (5.4)$$

where:

$$\left(\frac{m_{initial}}{m_{final}} \right) = \frac{m_{dry} + m_{pay} + m_{fuel}}{m_{dry} + m_{pay}}$$

I_{sp} is the specific impulse of the rocket engine (sec)

g_0 = gravitational acceleration at sea level = $9.81 \frac{m}{s^2}$

This expression can be further refined into an expression for the propellant mass-fraction (P_{mf}):

$$\frac{m_{dry} + m_{pay} + m_{fuel}}{m_{dry} + m_{pay}} = \frac{m_{dry} + m_{pay}}{m_{dry} + m_{pay}} + \frac{m_{fuel}}{m_{dry} + m_{pay}} = 1 + P_{mf} \quad (5.5)$$

With some simple algebraic manipulation, we come up with the following expression for the rocket equation in terms of the P_{mf} :

$$P_{mf} = \left[e^{\left(\frac{\Delta V}{I_{sp} \cdot g_0} \right)} - 1 \right] \quad (5.6)$$

The I_{sp} of the AKM's engine is assumed to be 300 sec. Substituting this into the above equation yields a numeric fraction for the amount of fuel required:

$$P_{mf} = \left[e^{\left(\frac{0.9230 \frac{km}{s}}{(300s) \left(.00981 \frac{km}{s^2} \right)} \right)} - 1 \right] = 0.368$$

With a mission payload mass of 4000kg, the amount of fuel required to produce the necessary “delta-V” to circularize the orbit is:

$$m_{fuel} + \frac{m_{fuel}}{0.368} = 4000kg \Rightarrow m_{fuel} = \frac{4000kg}{3.717} = 1076.14kg$$

D. ATLAS III-SCRAM

1. Configuration Data

The Atlas III-Scramjet (Figure 5.10) design shares the same 1st stage as the conventional Atlas III launch vehicle. That is where the design changes radically from the Atlas III. The second stage of the Atlas III-SCRAM incorporates a notional axis-symmetric scramjet design. The engine is mounted ahead of the payload module. Once first stage burnout occurs, the scramjet will in-effect function as a tugboat, pulling the payload into space.



Atlas III-SCRAM

Height:	28.91m
Diameter:	3.05m
Total Launch Mass:	93,752kg
Dry Mass:	20,807kg
Pmf:	3.51

Figure 5.10 Atlas III-SCRAM

2. Trajectory Design

Again, re-supply of the ISS was chosen as the baseline mission for analysis purposes. A target orbit of 425km was selected. In addition, a Low Earth Orbit (LEO) mission was chosen in an effort to showcase the operational flexibility of a scramjet-enabled launch vehicle. For this mission, an orbital altitude of 165km was chosen.

In order for a scramjet to operate in the most efficient manner, it is necessary for the vehicle to fly a constant pressure profile. The piloted simulation enabled rapid investigation of candidate profiles to be investigated in the time it would take conventional trajectory programs to test a single design. Once an intuitive feel was obtained, smarter starting values for autopilot weights, and waypoint selection could be rapidly achieved.

Figure 5.11 describes the trajectory for the Atlas III-SCRAM in terms of Mach #, and altitude. It is important to understand what information the figure is describing. As the vehicle passes through the Stratosphere (~45km), the temperature of the air drops rapidly. This leads to a decreased sonic velocity and (recalling Equation 2.2) therefore an increase in Mach #. The target point for stage one burnout and waypoints used are depicted in Figure 5.12. The autopilot initial values and weighting factors used in the trajectory design are shown in figure 5.13. These are valid for both of the trajectories as the scramjet flies a constant pressure profile.

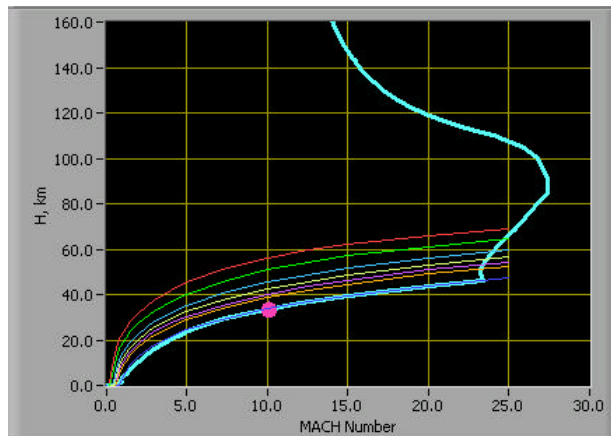


Figure 5.11 Atlas III-SCRAM Trajectory

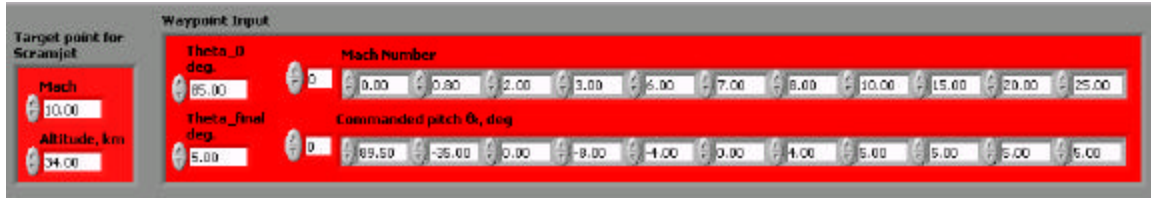


Figure 5.12 Autopilot Waypoint Values

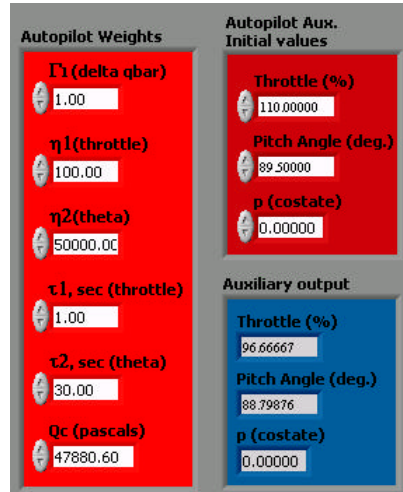


Figure 5.13 Autopilot Weights/Initial Values

3. ISS Mission Highlights

The ISS servicing mission necessitated specific fuel loading for both the first and second stages of the Atlas III-SCRAM. Fuel had to be offloaded from the first stage in order to achieve the pressure profile for the scramjet, without over stressing the vehicle. Figure 5.14 depicts the propulsion characteristics for the first stage. Figure 5.15 depicts the same information for the second stage (scramjet).

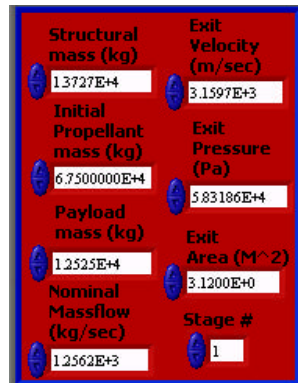


Figure 5.14 Stage One Propulsion Data

Structural mass (kg)	Exit Velocity (m/sec)
3.0800E+3	8.4870E+3
Initial Propellant mass (kg)	Exit Pressure (Pa)
5.0767000E+3	0.00000E+0
Payload mass (kg)	Exit Area (M ²)
4.0000E+3	1.0700E+0
Nominal Massflow (kg/sec)	Stage #
1.5000E+2	2

Figure 5.15 Stage Two Propulsion Data

a. Stage 1 Burnout

Figure 5.16 depicts the altitude/velocity profile of the Atlas III-SCRAM at the time of stage one burnout. Stage one burnout occurs at an altitude of 33.6463km. At the time of engine burnout, the Atlas III-SCRAM is traveling at Mach 10.3259 (3.16151km/s). The vehicle has traveled a downrange distance of 87km.

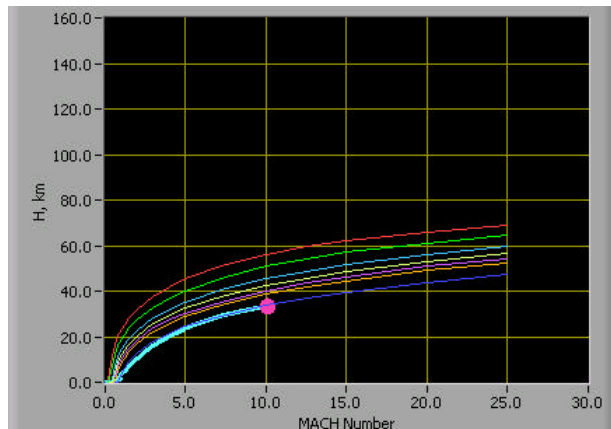


Figure 5.16 ISS Mission Stage One Burnout

b. Stage 2 Burnout

Figure 5.17 depicts the altitude/velocity profile of the Atlas III-SCRAM at the time of stage two burnout. Stage two burns out at an altitude of 45.9466km. At the time of engine burnout, the Atlas III-SCRAM is traveling at Mach 23.4387 (7.69348km/s). The vehicle has traveled a total downrange distance of 417km. Appendix B provides a comparative table of performance data for both the Atlas III and Atlas III-SCRAM vehicles. Although the scramjet burned out at a lower altitude and Mach number, it's velocity was greater by almost 1 km/s, and it's total specific energy is higher than the conventional Atlas III at this same point.

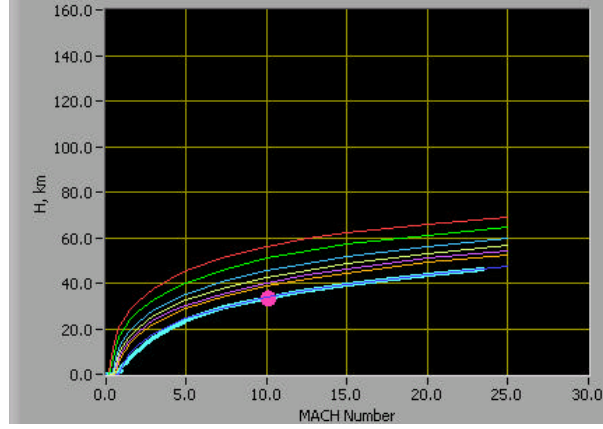


Figure 5.17 ISS Mission Stage Two Burnout

c. Apogee Burn

Once the second stage burns out, the remaining mission payload enters a coast phase. Airspeed is traded for altitude until the payload reaches the apogee altitude of 425 km (Figure 5.18). For the target altitude, $V_r \cong 0$, and $V_n = 7.539123 \frac{km}{s}$.

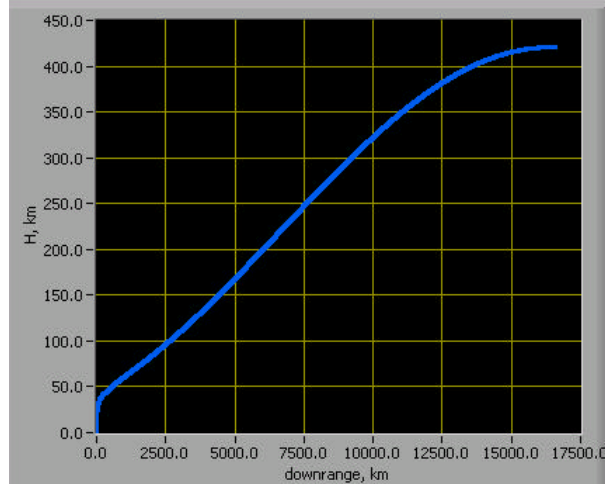


Figure 5.18 ISS Mission Apogee Altitude

We find that the “delta-V” necessary to circularize the final orbit at ISS mean orbital altitude is:

$$\Delta V = \sqrt{0 + \left(7.539123 \frac{km}{s} - \sqrt{\frac{3.986 \times 10^5 \frac{km^3}{s^2}}{(6371 + 425.01) km}} \right)^2} = 0.11934 \frac{km}{s}$$

This results in a P_{mf} of:

$$P_{mf} = \left[e^{\left(\frac{.11934 \frac{km}{s}}{(300s) \left(.00981 \frac{km}{s^2} \right)} \right)} - 1 \right] = 0.04138$$

Finally, it is determined that the amount of fuel needed to stabilize at a final orbital altitude of 425km is:

$$m_{fuel} + \frac{m_{fuel}}{0.04138} = 4000kg \Rightarrow m_{fuel} = \frac{4000kg}{25.166} = 158.943kg$$

4. LEO Mission Highlights

For the LEO example, fuel loading of the scramjet stage was selected in order to deliver the vehicle's payload into an orbit with a 165km apogee altitude. Figure 5.19 depicts the propulsion characteristics for the first stage. Figure 5.20 depicts the same information for the second stage (scramjet). Once again, the amount of “delta-V” achieved at stage one and stage two burnout is given. Also, the final velocity change to circularize the final orbit is determined.

Structural mass (kg)	Exit Velocity (m/sec)
1.3727E+4	3.1597E+3
Initial Propellant mass (kg)	Exit Pressure (Pa)
6.7000000E+4	5.83186E+4
Payload mass (kg)	Exit Area (M^2)
1.2525E+4	3.1200E+0
Nominal Massflow (kg/sec)	Stage #
1.2562E+3	1

Figure 5.19 Stage One Propulsion Data

Structural mass (kg)	Exit Velocity (m/sec)
3.0800E+3	8.4870E+3
Initial Propellant mass (kg)	Exit Pressure (Pa)
4.950000E+3	0.00000E+0
Payload mass (kg)	Exit Area (M^2)
4.0000E+3	1.0700E+0
Nominal Massflow (kg/sec)	Stage #
1.5000E+2	2

Figure 5.20 Stage Two Propulsion Data

a. Stage 1 Burnout

Figure 5.21 depicts the altitude/velocity profile of the Atlas III-SCRAM at the time of stage one burnout. Stage one burnout occurs at an altitude of 33.7639km. At the time of engine burnout, the Atlas III-SCRAM is traveling at Mach 10.3806 (3.181km/s). The vehicle has traveled a downrange distance of 87km.

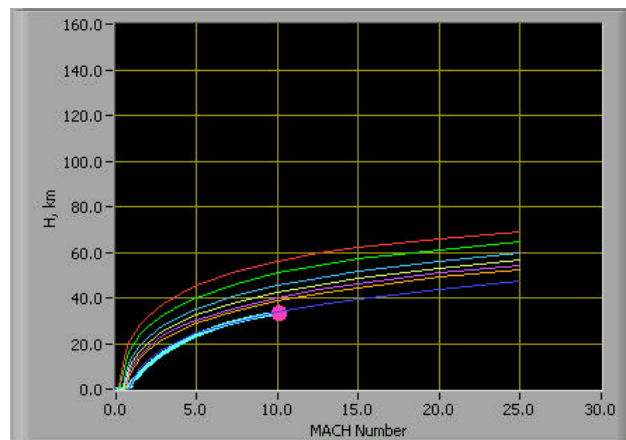


Figure 5.21 LEO Mission Stage One Burnout

b. Stage 2 Burnout

Figure 5.22 depicts the altitude/velocity profile of the Atlas III-SCRAM at the time of stage two burnout. Stage two burns out at an altitude of 45.9466km. At the time of engine burnout, the Atlas III-SCRAM is traveling at Mach 23.2849 (7.63842km/s). The vehicle has traveled a total downrange distance of 420km.

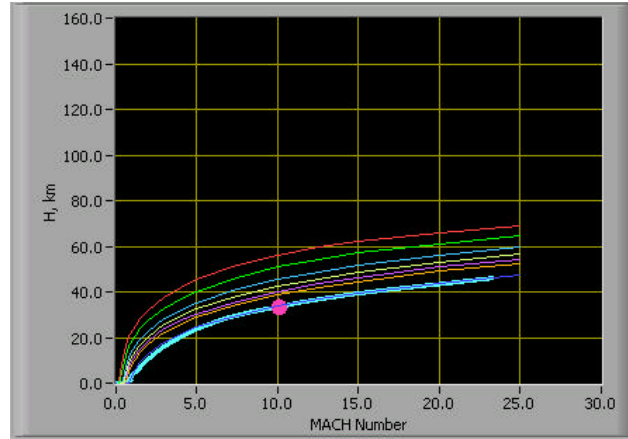


Figure 5.22 LEO Mission Stage Two Burnout

c. Apogee Burn

Once the second stage burns out, the remaining mission payload enters a coast phase. Airspeed is traded for altitude until the payload reaches the apogee altitude of 165km (Figure 5.23).

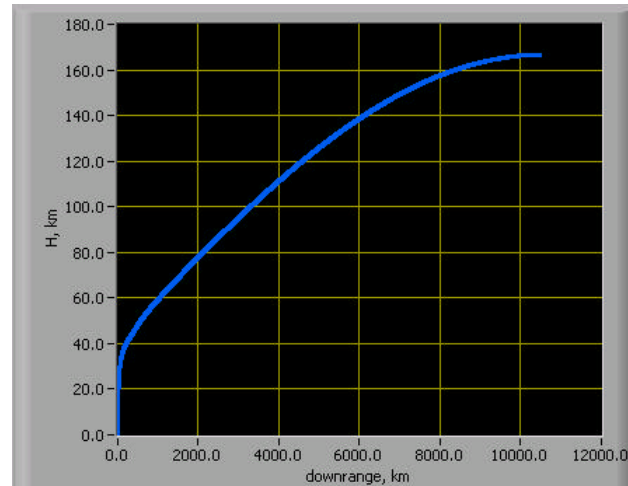


Figure 5.23 LEO Mission Apogee Altitude

At apogee, $V_r \cong 0$, and $V_n = 7.738096 \frac{km}{s}$. Substituting numerical values into the previously presented equation yields the following expression for the required “delta-V”:

$$\Delta V = \sqrt{0 + \left(7.738096 \frac{km}{s} - \sqrt{\frac{3.986 \times 10^5 \frac{km^3}{s^2}}{(6371 + 165) km}} \right)^2} = 0.0712 \frac{km}{s}$$

Now that we know the amount of “delta-V” necessary to circularize our final orbit, the amount of fuel required for this task must be determined. The I_{sp} of the vehicle’s engine is assumed to be 300 sec. Substituting this into the equation for P_{mf} yields a numeric fraction for the amount of fuel required:

$$P_{mf} = \left[e^{\left(\frac{\left(\frac{.0712 \frac{km}{s}}{(300s) \left(.00981 \frac{km}{s^2} \right)} \right)} \right)} - 1 \right] = 0.0245$$

With a mission payload mass of 4000kg, the amount of fuel required to produce the necessary “delta-V” to circularize the orbit is:

$$m_{fuel} + \frac{m_{fuel}}{0.0245} = 4000kg \Rightarrow m_{fuel} = \frac{4000kg}{41.816} = 95.7kg$$

E. CONCLUSIONS

1. Performance Basis

The scramjet-enabled design is inherently more flexible than the conventional Atlas III design. With a small increase in fuel for the scramjet stage, apogee altitude can be raised by a factor of more than 2.5. This enables the Atlas III-SCRAM design to deliver payloads to orbital altitudes throughout LEO and into the beginning of the MEO region. The Atlas III is designed to inject payloads into geo-transfer orbits (GTO). The station-servicing scenario assumes that the Centaur upper stage of the Atlas III can be defueled by the described amount, without an adverse affect upon the vehicle’s stability. Table 5.1 summarizes the orbital insertion requirements for the two designs with respect to the different orbital profiles.

	Atlas III/ SCRAM	Atlas III/ SCRAM	Atlas III
Apogee Alt. (km)	165	425	425
Prop. Mass Fraction	0.0245	0.04138	0.368
Prop. Mass (kg)	95.7	158.943	1076.02

Table 5.1 Final Orbit Insertion Requirements

In the envisioned launch configurations for each vehicle, the Atlas III-SCRAM would have a total launch mass of 93,752kg, compared to a launch mass of 177,807kg for the Atlas III. The Atlas III-SCRAM would have a higher dry mass (20,807kg) than the Atlas III (19,907kg). This is due to the weight of the scramjet module and associated support systems. P_{mf} for the Atlas III-SCRAM is calculated as $P_{mf} = 3.51$. The Atlas III, sitting on the launch pad, has a $P_{mf} = 7.93$. Table 5.2 summarizes the above results. The greater dry mass for the Atlas III-SCRAM accounts for the weight of thermal protection.

	Atlas III-SCRAM	Atlas III
Total Launch Mass (kg)	93,752	177,807
Dry Mass (kg)	20,807	19,907
Prop. Mass Fraction	3.51	7.93

Table 5.2 Comparison of Launcher Characteristics

2. Economic Basis

There is a rule of thumb that says that launch vehicle cost is proportional to the propellant mass fraction. This provides a back-of-the-envelope check when determining launch vehicle cost. This is only useful as a rough-cut for budgetary exercises.

Based upon open source information, the Federal Aviation Administration (FAA) estimates a price range for commercial Atlas III launch services of \$90-105 million [AIAA 3rd Edition]. Lockheed Martin has previously absorbed the development costs of the Atlas III. The development costs of the scramjet-enabled design could be in the range of \$700-900 million [Davis]. Until commercial customers consider the design “mature”, it is likely that the cost per launch of the Atlas III-SCRAM design would exceed that of the Atlas III.

It is difficult to determine what, if any thing would be gained by incorporating reusability into the Atlas III-SCRAM design. The assumption is made that since Lockheed-Martin did not incorporate reusable features into its Atlas III, the judgment must have been made that this offered very little return on investment. This does not preclude incorporating reusability into the Atlas III-SCRAM design, but it does provide a starting point for design features.

3. Censere Universus

It has been shown that fuel and oxidizer are the two greatest components of the weight of a launch vehicle. Inclusion of a scramjet removes the need to carry oxidizer for combustion of the fuel. By virtue of this, I_{sp} is increased by a factor of 7, dependent upon the fuel mixture used. Equivalently, using atmospheric oxygen as the oxidizer allows the engine to produce the same amount of thrust while using 1/7 the amount of propellant.

The scramjet-enabled design was able to deliver the mission payload to a variety of orbits, with a total launch vehicle mass much less than the standard Atlas III. What falls out of this analysis is that scramjets provide the potential to put larger customer payloads into orbit than are possible with a conventional design, or that a scramjet-enabled vehicle that has a much smaller first stage can loft the same payload as larger conventional configurations.

Because it is unlikely that NASA would be able to dedicate the funds necessary to establish a new scramjet development program, it will be necessary for industry to do so. Until the commercial launch sector determines that it is in their best interest to deviate from the conventional means of building rockets, the performance benefits of scramjet technology will not be realized, or leveraged in an effort to reduce the cost of space launch.

VI. FUTURE WORK

A. INTRO

This thesis addressed the feasibility of incorporating scramjet technology into an expendable launch vehicle. In order for this vision to become reality, further research is needed in the areas of Computational Fluid Dynamics (CFD), vehicle stability, as well as thermal/acoustic stresses and dynamic loading.

The primary concerns are vehicle controllability, the stresses such a vehicle would experience throughout the flight envelope, and the thermal loading it would experience during long duration high-speed flight through the atmosphere.

Equally as important as the areas of further research that address whether “we can do it,” is research that addresses how such technology would be applied. It is left to future students to determine operational concepts in which the scramjet might offer

B. SCRAMJET DEVELOPMENT PROGRAM

In order to realize the performance potential of incorporating a scramjet into a launch vehicle stack, a comprehensive program must be developed. This effort would likely be a multi-national one, taking advantage of the various geographic, political, and technological strengths of each partner.

The X-15 high-speed flight test program has contributed to the success of US space activities from the Apollo Lunar program to the Shuttle Orbiter. One reason it was such a success, was the rate at which flights were conducted. Almost 200 flights were conducted between the time that the program started in 1959, and the time of the final on October 24, 1968. In order to gather a similar volume of data regarding flight in the hypersonic region, a flight schedule on the order of 20 flights a year would be necessary.

This would also require a shift from the “zero-defect” mentality that exists today in the aerospace industry. The airplane did not make the jump from the Wright Brothers Flyer to the F-22 Raptor overnight. Small incremental improvements were made over time, and numerous failures occurred along the way. A test-fly-fix-fly (TF³) approach would still apply strict attention to detail, but would allow for the pursuit of several different development paths at the same time.

Another idea that could be incorporated would be to adapt surplus munitions that are being retired by the military. The F-14 Tomcat is scheduled to leave the fleet within the next 10 years [F-14]. The aircraft serves the Navy in an air superiority, fleet defense, and precision strike role. One of the many different weapons the Tomcat can employ is the AIM-54 missile, code-named “Phoenix.” The Phoenix missile is the Navy's only long-range air-to-air missile. Table 6.1 gives the general characteristics of the Phoenix missile. By modifying the guidance systems of the Phoenix, it should be possible to enable the missile to arrive at a particular point in the sky. This would enable it to fulfill the role of a high-speed flight test vehicle.

Primary Function:	Long-range air-launched air intercept missile
Contractor:	Hughes Aircraft Co. and Raytheon Co.
Unit Cost:	\$477,131
Power Plant:	Solid propellant rocket motor built by Hercules
Length:	13 feet (3.9 meters)
Weight:	1,024 pounds (460.8 kg)
Diameter:	15 inches (38.1 cm)
Wing Span:	3 feet (.9 meters)
Range:	In excess of 100 nautical miles (115 statute miles, 184 km)
Speed:	In excess of 3,000 mph (4,800 kmph)
Guidance System:	Semi-active and active radar homing
Warheads:	Proximity fuse, high explosive
Warhead Weight:	135 pounds (60.75 kg)
Date Deployed:	1974

Table 6.1 AIM-54 (Phoenix) Characteristics

An axis-symmetric scramjet design would be the best suited for this type of test vehicle. The designers do not have to contend with the asymmetric loads associated with body-integrated designs. The design also helps mitigate the heat build up that will result from travel through the atmosphere.

VII. SUMMARY

The goal of this thesis research was to determine the feasibility of scramjet technology for an intermediate propulsive stage of an expendable launch vehicle. The reader was first provided with a review of basic concepts necessary for a better understanding of the assertions made within the thesis. Next a quick overview of US and international scramjet research efforts was undertaken to provide a broader context. Detailed information regarding the software programs selected for the development of the analysis tools, and how these tools were utilized will enable interested parties to reproduce and validate the conclusions of this thesis.

Scramjet technology provides a potential means of significantly reducing the cost of delivering payloads to orbit. Using atmospheric oxygen as the oxidizer allows the engine to produce the same amount of thrust while carrying 1/7 the amount of propellant as conventional rocket engines. However these benefits do not come cheaply. Scramjets deliver far higher I_{sp} values, but they must follow an air-breathing trajectory. Aerodynamic heating and drag become significant issues. The extra mass required for heat protection takes away from the payload fraction. Nonetheless, this analysis shows significant potential gains for the scramjet configuration.

A scramjet-enabled vehicle enjoys greater operational flexibility than conventional designs. The final orbit of a payload delivered by such a vehicle is theoretically only limited by the performance of the scramjet stage. By varying the duration of flight within the atmosphere, useful payload weights can be delivered to practically any orbital regime. By focusing efforts upon expendable vehicle designs, these benefits can be realized in the short-term.

Pursuit of an axis-symmetric design could leverage current international research efforts in supersonic combustion, and avoid the stability and control issues that plague body-integrated designs. The concepts proposed in this thesis are approaching a technology readiness level (TRL) at which potential applications of an axis-symmetric design could be found in the very near term.

THIS PAGE INTENTIONALLY LEFT BLANK

APPENDIX A. DERIVATION OF ALGORITHMIC EQUATIONS

Back in Chapter IV (Launch Simulation), the equations of motion used in the launch simulation were derived. What remains is to develop the six classical orbital elements (COEs). Once this is done, rotational matrices will be derived to shift from the orbital to the inertial plane. Finally, the conditions used to initialize the simulation are calculated.

The order of presentation may at first seem counter intuitive, but the choice is completely arbitrary. In the LabView code, in order to project the ground track of the vehicle, it is necessary to go from the perifocal to the inertial frame for each data frame. To initialize the simulation, the order of steps is reversed.

A. DERIVATION OF CLASSIC ORBITAL ELEMENTS

Once an expression is obtained for the position and velocity vectors in the orbital plane, the next step is to derive the six classic orbital elements (COEs): $a, e, i, \mathbf{w}, \mathbf{\Omega}, \mathbf{n}$ that define the vehicle's orbit. All that is needed is the vehicle's inertial position and velocity, $\bar{\mathbf{R}}$ and $\bar{\mathbf{V}}$. *Understanding Space*, by Jerry Sellers provides an in-depth explanation for derivation of the COEs.

1. Semi-major Axis, a

In order to determine the semi-major axis of the orbit, the magnitude of the position and velocity vectors are used. The Vis-Viva equation gives an expression for the semi-major axis

$$a = \frac{\mathbf{m}}{\frac{2 \cdot \mathbf{m}}{R} - V^2} \quad (\text{A.1})$$

where: $R = \text{magnitude of the position vector (km)} = \sqrt{R_x^2 + R_y^2 + R_z^2} \quad (\text{A.2})$

$$V = \text{magnitude of the velocity vector} \left(\frac{\text{km}}{\text{sec}} \right) = \sqrt{V_x^2 + V_y^2 + V_z^2} \quad (\text{A.3})$$

$$\mathbf{m} = \text{earth's gravitational parameter} = 3.986 \times 10^5 \left(\frac{\text{km}^3}{\text{sec}^2} \right)$$

In order for the orbit to be viable, the value of the semi-major axis should be larger than the radius of the planet it is orbiting.

2. Eccentricity, e

The eccentricity vector \vec{e} relates to the position and velocity vectors by the expression

$$\vec{e} = \frac{1}{m} \left[\left[V^2 - \frac{m}{R} \right] \cdot \vec{R} - [\vec{R} \cdot \vec{V}] \cdot \vec{V} \right] \quad (\text{A.4})$$

where: $m = \text{earth's gravitational parameter} = 3.986 \times 10^5 \left(\frac{\text{km}^3}{\text{sec}^2} \right)$

3. Inclination, i

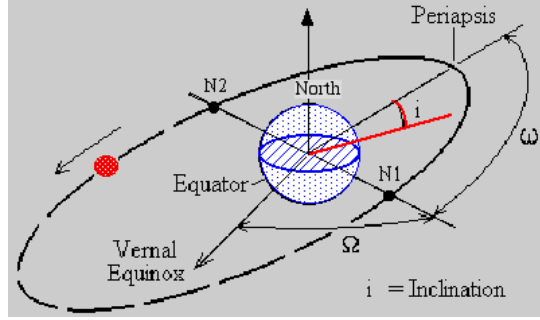


Figure A.1 Inclination

Inclination defines the orientation of the orbit with respect to the Earth's equatorial plane. It is the angle between the unit vector, \hat{K} , through the North Pole, and the angular momentum vector, \vec{h} .

$$i = \cos^{-1} \left[\frac{\hat{K} \cdot \vec{h}}{K \cdot h} \right] \quad (\text{A.5})$$

The angular momentum vector, \vec{h} , is obtained by taking the cross product of the position and velocity vectors.

$$\vec{h} = \vec{R} \times \vec{V} \quad (\text{A.6})$$

4. Right Ascension of the Ascending Node, W

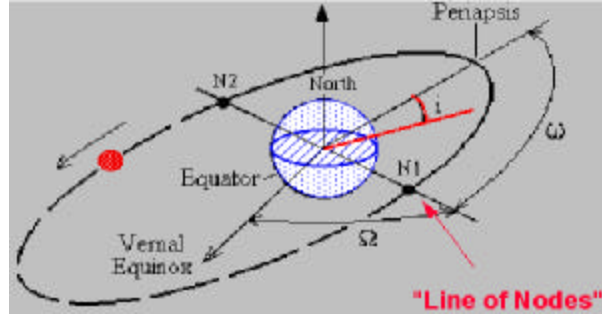


Figure A.2 Right Ascension of the Ascending Node

The right ascension of the ascending node (RAAN) defines the point at which the orbital plane crosses the equatorial plane. It is the angle measured from the vector defining the 1st point of Aries, \hat{I} , and the ascending node of the orbit. The ascending node vector, \bar{n} , lies in the equatorial plane, is perpendicular to the polar axis, \hat{K} , and is perpendicular to the angular momentum vector, \bar{h} .

$$\bar{n} = \hat{K} \times \bar{h} \quad (\text{A.7})$$

The dot product is used to determine Ω (the angle between \hat{I} and \bar{n})

$$\Omega = \cos^{-1} \left(\frac{\hat{I} \cdot \bar{n}}{I \cdot n} \right) \quad (\text{A.8})$$

Because RAAN can range between 0° and 360° , it is necessary to perform a quadrant check. Figure A.2 shows the relationship of the ascending node vector and geocentric equatorial coordinate system. The quadrant can be determined by inspection of the position of the ascending node vector relative to the \hat{J} unit vector. If $(\hat{J} \cdot \bar{n}) \geq 0$, then $0 \leq \Omega \leq 180^\circ$. Otherwise, $180 \leq \Omega \leq 360^\circ$.

5. Argument of Perigee, w

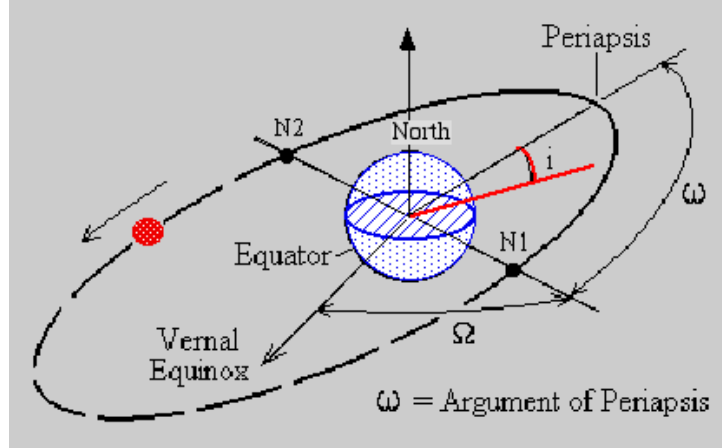


Figure A.3 Argument of Perigee

The argument of perigee defines the periaapsis (low point) of the orbit relative to a fixed line in inertial space. It is measured as the angle between the ascending node vector and the eccentricity vector. Using the dot product yields the expression for w

$$w = \cos^{-1} \left(\frac{\bar{n} \cdot \bar{e}}{n \cdot e} \right) \quad (\text{A.9})$$

The following logical relationship determines the correct quadrant for w

$$\text{If } (\hat{K} \cdot \bar{e}) \geq 0$$

$$0 \leq w \leq 180^\circ$$

Else

$$180 \leq w \leq 360^\circ$$

6. True Anomaly, n

True anomaly is defined as the angle between the eccentricity vector, \bar{e} , and the position vector \bar{R}

$$n = \cos^{-1} \left(\frac{\bar{e} \cdot \bar{R}}{e \cdot R} \right) \quad (\text{A.10})$$

It is also possible to derive an expression for the true anomaly in terms of the semi-major axis.

$$r = \frac{a[1-e^2]}{1+e \cdot \cos(\mathbf{n})} \Rightarrow \mathbf{n} = \cos^{-1} \left[\frac{1}{e} \left[\frac{a[1-e^2]}{R} \right] - 1 \right] \quad (\text{A.11})$$

B. COORDINATE SYSTEM TRANSFORMATION

The inertial reference axis is a line that defines a fixed axis system with respect to inertial space. Figure A.4 depicts the right-handed XYZ coordinate system. The x-axis

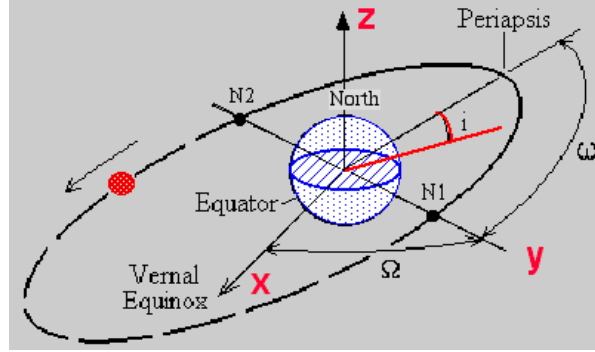


Figure A.4 XYZ Coordinate System

points in the direction of the vernal equinox, which serves as the “anchor” for the coordinate system. The z-axis passes through the geographic north pole of the Earth. The y-axis completes the system. All axes are perpendicular to each other.

Given the COE set, the vehicle’s position with respect to the inertial axes can be computed through the use of rotational matrices. Vallado, in Fundamentals of Astrodynamics & Applications, provides a rigorous derivation of the transformation from the orbital frame to the inertial frame.

1. Position Vector (Inertial Frame)

A 3x1 matrix represents the position vector in the inertial frame, where

$$\begin{bmatrix} x \\ y \\ z \end{bmatrix} = R \begin{bmatrix} \cos(\mathbf{n} + \mathbf{w}) \cos(\Omega) - \sin(\mathbf{n} + \mathbf{w}) \cos(i) \sin(\Omega) \\ \cos(\mathbf{n} + \mathbf{w}) \sin(\Omega) + \sin(\mathbf{n} + \mathbf{w}) \cos(i) \cos(\Omega) \\ \sin(\mathbf{n} + \mathbf{w}) \sin(i) \end{bmatrix} \quad (\text{A.12})$$

2. Velocity Vector (Inertial Frame)

The following matrix gives the velocity vector in the inertial frame

$$\begin{bmatrix} V_x \\ V_y \\ V_z \end{bmatrix} = \sqrt{\frac{m}{a[1-e^2]}} \times \quad (\text{A.13})$$

$$\begin{bmatrix} -\left[\cos(\Omega)\left[e\sin(\mathbf{w}) + \sin(\mathbf{n} + \mathbf{w})\right] + \cos(i)\left[e\cos(\mathbf{w}) + \cos(\mathbf{n} + \mathbf{w})\right]\sin(\Omega)\right] \\ \cos(i)\left[e\cos(\mathbf{w}) + \cos(\mathbf{n} + \mathbf{w})\right]\cos(\Omega) - \left[e\sin(\mathbf{w}) + \sin(\mathbf{n} + \mathbf{w})\right]\sin(\Omega) \\ \left[e\cos(\mathbf{w}) + \cos(\mathbf{n} + \mathbf{w})\right]\sin(-i) \end{bmatrix}$$

C. ESTABLISHING INITIAL CONDITIONS

To start, it is necessary to define the initial conditions at launch. Launch position will be defined in terms of latitude, inertial longitude, and altitude. Figure A.5 graphically depicts the launch position in the Earth centered frame of reference.

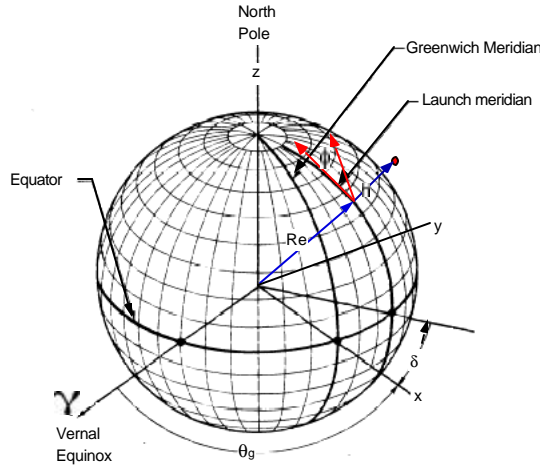


Figure A.5 Geocentric Launch Position

1. Position Vector

In the inertial coordinate system, the launch position in matrix form is

$$\begin{bmatrix} R_x \\ R_y \\ R_z \end{bmatrix}_{\text{Inertial}} = \begin{bmatrix} [R_{\text{earth}} + h_0] \cdot \cos[I_0] \cdot \cos[d_0] \\ [R_{\text{earth}} + h_0] \cdot \cos[I_0] \cdot \sin[d_0] \\ [R_{\text{earth}} + h_0] \cdot \sin[I_0] \end{bmatrix} \quad (\text{A.14})$$

where:

- R_{earth} is the radius of the earth (km)
- h_0 is launch altitude (km)
- I_0 is launch latitude (deg)
- d_0 is launch inertial longitude (deg)

Within the simulation, the radius of the earth was described as a function of latitude. By considering the earth as an ellipsoid, the radius at any point can be described in terms of its semi-major and semi-minor axes. Figure A.6 depicts the relationship of latitude to position on the surface of the ellipse.

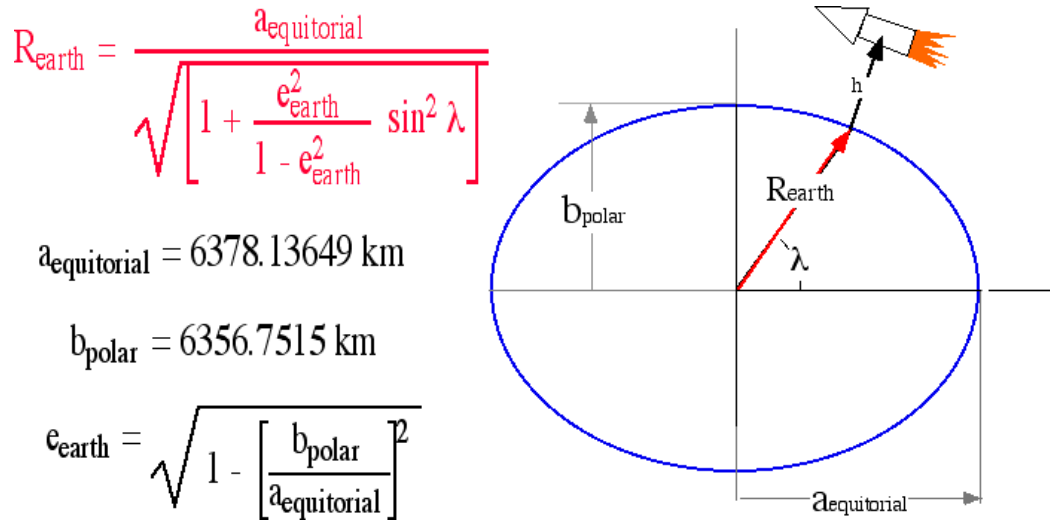


Figure A.6 Ellipsoidal Earth Model

2. Velocity Vector

It is desirable to input the velocity in terms of a natural set of coordinates referenced to the vehicle's flight path. The velocity vector in polar coordinates is

$$\vec{V} \rightarrow \begin{bmatrix} V_0 \\ g \\ f \end{bmatrix} \quad (A.15)$$

where

- V_0 = Earth relative velocity $\left(\frac{km}{sec}\right)$
- g = flight path angle (deg)
- f = launch azimuth (deg)

The flight path angle is referenced to the local horizon. It is the angle between the velocity vector and the local horizon. The launch azimuth is referenced from due north.

The velocity vector can be further expressed in terms of its components

$$\begin{bmatrix} V_{north} \\ V_{east} \\ V_{down} \end{bmatrix} = \begin{bmatrix} V_0 \cos(\mathbf{f}) \cos(\mathbf{g}) \\ V_0 \sin(\mathbf{f}) \cos(\mathbf{g}) \\ -V_0 \sin(\mathbf{g}) \end{bmatrix} + \begin{matrix} \text{Rotational velocity} \\ \text{of Earth} \end{matrix} \quad (\text{A.16})$$

The boost in velocity due to the rotation of the Earth acts due east, and is expressed as

$$V_{Earth(boost)} = [\mathbf{R}_{earth} + h_0] \cdot [\Omega_{earth} \cos(\mathbf{I}_0)] \quad (\text{A.17})$$

where:

$$\Omega_{earth} = \text{Earth angular velocity} \left(\frac{rad}{sec} \right) = .00007292115 \frac{rad}{sec}$$

In order to get to the inertial frame, two successive rotations are accomplished. The final form of the velocity vector (considering the characteristics of the launch site) is

$$\begin{bmatrix} V_x \\ V_y \\ V_z \end{bmatrix}_{Inertial} = \begin{bmatrix} -\cos(\mathbf{d}_0) \sin(\mathbf{I}_0) & -\sin(\mathbf{d}_0) & -\cos(\mathbf{d}_0) \cos(\mathbf{I}_0) \\ -\sin(\mathbf{d}_0) \sin(\mathbf{I}_0) & \cos(\mathbf{d}_0) & -\sin(\mathbf{d}_0) \cos(\mathbf{I}_0) \\ \cos(\mathbf{I}_0) & 0 & -\sin(\mathbf{I}_0) \end{bmatrix} \cdot \begin{bmatrix} V_0 \cos(\mathbf{f}) \cos(\mathbf{g}) \\ V_0 \sin(\mathbf{f}) \cos(\mathbf{g}) + [\mathbf{R}_{earth} + h_0] \Omega_{earth} \cos(\mathbf{I}_0) \\ -V_0 \sin(\mathbf{g}) \end{bmatrix} \quad (\text{A.18})$$

APPENDIX B. COMPARISION OF ISS MISSION ATLAS III/ ATLAS III-SCRAM PERFORMANCE CHARACTERISTICS

The following tables provide the reader with reference tool for comparing the Atlas III and the Atlas III-SCRAM's performance during the ISS re-supply mission. The selected data points include the initial mass and fuel mass for stage one and two, as well as the altitude and velocity at which stage burnout occurred.

A. ATLAS III

Atlas III	Initial Mass (kg)	Propellant Mass (kg)
Stage One	177,807	1.5190E+05
Stage Two	9,405	3.2250E+03

Table B.1 Atlas III Mass Properties

Atlas III	Burnout Alt. (km)	Velocity (Mach)	Velocity (km/s)
Stage One	81.0466	17.879	4.999
Stage Two	95.538	24.3619	6.75

Table B.2 Atlas III Performance Characteristics

B. ATLAS III-SCRAM

Atlas III-SCRAM	Initial Mass (kg)	Propellant Mass (kg)
Stage One	93,752	6.7500E+04
Stage Two	12,157	5.0767E+03

Table B.3 Atlas III-SCRAM Mass Properties

Atlas III-SCRAM	Burnout Alt. (km)	Velocity (Mach)	Velocity (km/s)
Stage One	33.6463	10.3259	3.16151
Stage Two	45.9466	23.4387	7.69348

Table B.4 Atlas III-SCRAM Performance Characteristics

THIS PAGE INTENTIONALLY LEFT BLANK

APPENDIX C. AERODYNAMIC DATA

The following tables contain the aerodynamic data obtained from AeroCFD and HyperCFD for the notional launch vehicle. To facilitate easy understanding, the data were entered into Microsoft Excel.

A. SUBSONIC

All tables are to be read with alpha varying down the left side and values of Cd/Cn for Mach values of 0, .2, .5, .7, and .8 across the top.

Alpha	Cd(0)	Cd(.2)	Cd(.5)	Cd(.7)	Cd(.8)	Alpha	Cn(0)	Cn(.2)	Cn(.5)	Cn(.7)	Cn(.8)
0	1.688	1.709	1.844	2.099	2.383	0	0	0	0	0	0
1	1.688	1.709	1.843	2.098	2.382	1	2.801	2.858	3.234	3.922	4.668
2	1.688	1.709	1.843	2.098	2.382	2	2.865	2.924	3.308	4.012	4.775
3	1.689	1.71	1.844	2.098	2.382	3	2.996	3.058	3.46	4.196	4.994
5	1.698	1.718	1.853	2.106	2.388	5	3.458	3.529	3.993	4.842	5.763
8	1.74	1.76	1.894	2.145	2.425	8	4.631	4.726	5.347	6.485	7.718
10	1.797	1.817	1.951	2.201	2.478	10	5.718	5.836	6.602	8.006	9.529
15	2.091	2.112	2.244	2.491	2.762	15	9.396	9.589	10.849	13.156	15.659

Table C.1 Stage I/II (No delta correction)

Alpha	Cd(0)	Cd(.2)	Cd(.5)	Cd(.7)	Cd(.8)	Alpha	Cn(0)	Cn(.2)	Cn(.5)	Cn(.7)	Cn(.8)
0	0.574	0.582	0.636	0.737	0.847	0	0	0	0	0	0
1	0.574	0.582	0.636	0.737	0.847	1	1.758	1.794	2.03	2.462	2.93
2	0.574	0.582	0.636	0.737	0.847	2	1.787	1.824	2.063	2.502	2.978
3	0.575	0.583	0.637	0.738	0.848	3	1.842	1.88	2.127	2.579	3.07
5	0.582	0.59	0.644	0.744	0.853	5	2.03	2.072	2.344	2.843	3.384
8	0.611	0.619	0.672	0.771	0.879	8	2.5	2.551	2.886	3.5	4.166
10	0.649	0.657	0.71	0.808	0.915	10	2.93	2.991	3.384	4.103	4.884
15	0.839	0.847	0.899	0.994	1.098	15	4.376	4.466	5.053	6.128	7.293

Table C.2 Stage II (With Fins)

Alpha	Cd(0)	Cd(.2)	Cd(.5)	Cd(.7)	Cd(.8)	Alpha	Cn(0)	Cn(.2)	Cn(.5)	Cn(.7)	Cn(.8)
0	0.478	0.487	0.541	0.641	0.752	0	0	0	0	0	0
1	0.478	0.487	0.541	0.641	0.751	1	0.001	0.002	0.002	0.002	0.002
2	0.478	0.487	0.541	0.641	0.751	2	0.003	0.003	0.003	0.004	0.005
3	0.479	0.488	0.542	0.642	0.752	3	0.004	0.005	0.005	0.006	0.007
5	0.486	0.494	0.548	0.648	0.757	5	0.007	0.008	0.009	0.01	0.012
8	0.515	0.523	0.577	0.676	0.784	8	0.012	0.012	0.014	0.016	0.02
10	0.553	0.561	0.614	0.713	0.82	10	0.015	0.015	0.017	0.02	0.024
15	0.743	0.751	0.803	0.899	1.002	15	0.021	0.022	0.025	0.03	0.036

Table C.3 Stage II (No Fins)

Alpha	Cd(0)	Cd(.2)	Cd(.5)	Cd(.7)	Cd(.8)	Alpha	Cn(0)	Cn(.2)	Cn(.5)	Cn(.7)	Cn(.8)
0	0.096	0.095	0.095	0.096	0.095	0	0	0	0	0	0
1	0.096	0.095	0.095	0.096	0.096	1	1.757	1.792	2.028	2.46	2.928
2	0.096	0.095	0.095	0.096	0.096	2	1.784	1.821	2.06	2.498	2.973
3	0.096	0.095	0.095	0.096	0.096	3	1.838	1.875	2.122	2.573	3.063
5	0.096	0.096	0.096	0.096	0.096	5	2.023	2.064	2.335	2.833	3.372
8	0.096	0.096	0.095	0.095	0.095	8	2.488	2.539	2.872	3.484	4.146
10	0.096	0.096	0.096	0.095	0.095	10	2.915	2.976	3.367	4.083	4.86
15	0.096	0.096	0.096	0.095	0.096	15	4.355	4.444	5.028	6.098	7.257

Table C.4 Delta Calculation (B.2-B.3)

Alpha	Cd(0)	Cd(.2)	Cd(.5)	Cd(.7)	Cd(.8)	Alpha	Cn(0)	Cn(.2)	Cn(.5)	Cn(.7)	Cn(.8)
0	1.784	1.804	1.939	2.195	2.478	0	0	0	0	0	0
1	1.784	1.804	1.938	2.194	2.478	1	4.558	4.65	5.262	6.382	7.596
2	1.784	1.804	1.938	2.194	2.478	2	4.649	4.745	5.368	6.51	7.748
3	1.785	1.805	1.939	2.194	2.478	3	4.834	4.933	5.582	6.769	8.057
5	1.794	1.814	1.949	2.202	2.484	5	5.481	5.593	6.328	7.675	9.135
8	1.836	1.856	1.989	2.24	2.52	8	7.119	7.265	8.219	9.969	11.864
10	1.893	1.913	2.047	2.296	2.573	10	8.633	8.812	9.969	12.089	14.389
15	2.187	2.208	2.34	2.586	2.858	15	13.751	14.033	15.877	19.254	22.916

Table C.5 Launch Configuration (B.1+B.4)

B. SUPERSONIC

All tables are to be read with alpha varying down the left side and values of Cd/Cn for Mach values of 1.2, 1.5, 2, 5, 8, and 10 across the top.

Alpha	Cd(1.2)	Cd(1.5)	Cd(2)	Cd(5)	Cd(8)	Cd(10)	Alpha	Cn(1.2)	Cn(1.5)	Cn(2)	Cn(5)	Cn(8)	Cn(10)
0	1.0109	0.8888	0.7705	0.549	0.4947	0.4788	0	0	0	0	0	0	0
1	1.0109	0.8888	0.7705	0.549	0.4947	0.4788	1	0.24779	0.11631	0.09585	0.05786	0.048	0.04464
2	1.0109	0.8888	0.7705	0.549	0.4947	0.4788	2	0.49558	0.23261	0.1917	0.11571	0.096	0.08928
5	1.0109	0.8888	0.7705	0.549	0.4947	0.4788	5	1.23894	0.58153	0.47924	0.28929	0.24	0.22321
8	1.0109	0.8888	0.7705	0.549	0.4947	0.4788	8	1.9823	0.93045	0.76679	0.46286	0.38399	0.35713

Table C.6 Stage I/II (No Delta Correction)

Alpha	Cd(1.2)	Cd(1.5)	Cd(2)	Cd(5)	Cd(8)	Cd(10)	Alpha	Cn(1.2)	Cn(1.5)	Cn(2)	Cn(5)	Cn(8)	Cn(10)
0	0.9329	0.8461	0.699	0.4429	0.381	0.3625	0	0	0	0	0	0	0
1	0.9329	0.8461	0.699	0.4429	0.381	0.3625	1	0.24738	0.1159	0.09544	0.05745	0.04759	0.04424
2	0.9329	0.8461	0.699	0.4429	0.381	0.3625	2	0.49477	0.2318	0.19089	0.1149	0.09519	0.08847
5	0.9329	0.8461	0.699	0.4429	0.381	0.3625	5	1.23692	0.57951	0.47722	0.28726	0.23797	0.22118
8	0.9329	0.8461	0.699	0.4429	0.381	0.3625	8	1.97906	0.92721	0.76355	0.45962	0.38076	0.35389

Table C.7 Stage II (With Fins)

Alpha	Cd(1.2)	Cd(1.5)	Cd(2)	Cd(5)	Cd(8)	Cd(10)	Alpha	Cn(1.2)	Cn(1.5)	Cn(2)	Cn(5)	Cn(8)	Cn(10)
0	0.7544	0.6428	0.5678	0.3965	0.3523	0.3396	0	0	0	0	0	0	0
1	0.7544	0.6428	0.5678	0.3965	0.3523	0.3396	1	0.03031	0.03031	0.03031	0.03031	0.03031	0.03031
2	0.7544	0.6428	0.5678	0.3965	0.3523	0.3396	2	0.06062	0.06062	0.06062	0.06062	0.06062	0.06062
5	0.7544	0.6428	0.5678	0.3965	0.3523	0.3396	5	0.15155	0.15155	0.15155	0.15155	0.15155	0.15155
8	0.7544	0.6428	0.5678	0.3965	0.3523	0.3396	8	0.24248	0.24248	0.24248	0.24248	0.24248	0.24248

Table C.8 Stage II (No Fins)

Alpha	Cd(1.2)	Cd(1.5)	Cd(2)	Cd(5)	Cd(8)	Cd(10)	Alpha	Cn(1.2)	Cn(1.5)	Cn(2)	Cn(5)	Cn(8)	Cn(10)
0	0.1785	0.2033	0.1312	0.0464	0.0287	0.0229	0	0	0	0	0	0	0
1	0.1785	0.2033	0.1312	0.0464	0.0287	0.0229	1	0.21707	0.08559	0.06513	0.02714	0.01728	0.01393
2	0.1785	0.2033	0.1312	0.0464	0.0287	0.0229	2	0.43415	0.17118	0.13027	0.05428	0.03457	0.02785
5	0.1785	0.2033	0.1312	0.0464	0.0287	0.0229	5	1.08537	0.42796	0.32567	0.13571	0.08642	0.06963
8	0.1785	0.2033	0.1312	0.0464	0.0287	0.0229	8	1.73658	0.68473	0.52107	0.21714	0.13828	0.11141

Table C.9 Delta Calculation (B.7-B.8)

Alpha	Cd(1.2)	Cd(1.5)	Cd(2)	Cd(5)	Cd(8)	Cd(10)	Alpha	Cn(1.2)	Cn(1.5)	Cn(2)	Cn(5)	Cn(8)	Cn(10)
0	1.1894	1.0921	0.9017	0.5954	0.5234	0.5017	0	0	0	0	0	0	0
1	1.1894	1.0921	0.9017	0.5954	0.5234	0.5017	1	0.46486	0.2019	0.16098	0.085	0.06528	0.05857
2	1.1894	1.0921	0.9017	0.5954	0.5234	0.5017	2	0.92973	0.40379	0.32197	0.16999	0.13057	0.11713
5	1.1894	1.0921	0.9017	0.5954	0.5234	0.5017	5	2.32431	1.00949	0.80491	0.425	0.32642	0.29284
8	1.1894	1.0921	0.9017	0.5954	0.5234	0.5017	8	3.71888	1.61518	1.28786	0.68	0.52227	0.46854

Table C.10 Launch Configuration (B.6+B.9)

LIST OF REFERENCES

Aerospaceguide, "X-30 Aerospaceplane."

[<http://members.lycos.co.uk/spaceprojects/x-30.html>]. June 2002.

AIAA-96-4572, "Future Flight Test Plans of an Axisymmetric Hydrogen Fueled Scramjet Engine on the Hypersonic Flying Laboratory," by A.S. Roudakov, V.L. Semenov, V.I. Kopchenov, and J.W. Hicks, p. 1, November 1996

Airwise News, "China Developing Hypersonic Aircraft."

[<http://news.airwise.com/stories/2001/09/1000729094.html>]. September 2001.

Centre for Defense and International Security Studies, "Hypersonic Vehicles- Back to the Future."

[<http://www.cdiss.org/1>]. July 2000.

Centre for Defense and International Security Studies, "Hypersonic Vehicles: Current National Programs."

[<http://www.cdiss.org/hyper2.htm>]. July 2000.

Davis, Mark, NASA, 28 August 2002.

Edwards Air Force Base, "Test Flight of Hypersonic Plane Fails."

[<http://www.spacedaily.com/news/010602212602.h2y085tu.html>]. June 2001.

Fahroo, F. and Ross, I.M., "Direct Trajectory Optimization by a Chebyshev Pseudospectral Method," *American Control Conference*, Chicago, IL, June 2000.

Friedberger, W.F., "International Dictionary of Applied Mathematics.", pp.797-798, Van Nostrand Co. Inc., 1960.

International Reference Guide to Space Launch Systems, 3rd Edition, p. 273,
American Institute of Aeronautics and Astronautics, 1999.

Ibid, p.56.

Jane's Missiles and Rockets, "Hypersonic Missile Reaches Mach 6+ in Low-Level
Flight."

[[. March 2002.](http://www4.janes.com/search97cgi/s97_cgi?action=View&VdkVgwKey=/content1/janesdata/mags/jmr/jmr00189.htm&Collection=current&ViewTemplate=doc_view_jmr.htm&Prod_Name=JMR&)

McClinton, Charles R., "Air-Breathing Engines."

[[. February 1999.](http://www.sciam.com/article.cfm?articleID=000AE34D-EBB2-1CB8-B4A8809EC588EEDF)

Milnet, "Joint Warfighter DTOs Precision Force."

[[. January 1995.](http://www.milnet.com/milnet/pentagon/dto/jw_dto_b.htm)

NACA Report 1147, "The Similarity Law for Hypersonic Flow and Requirements for
Dynamic Similarity of Related Bodies in Free Flight," by F.M. Hamaker, S.E. Neice, and
T.J. Wong, June 1953.

NASA Glenn Research Center, "Combined Cycle Propulsion."

[[. January 2002.](http://www.grc.nasa.gov/WWW/AERO/base/ccp.htm)

NASA-TM-1998-206548, "Recent Flight Test Results of the Joint CIAM-NASA Mach
6.5 Scramjet Flight Program," by A.S. Roudakov, V.L. Semenov, and J.W. Hicks, p. 1,
April 1998.

National Aerospace Laboratory of Japan, "High Speed Flight Demonstration."

[[. March 2002.](http://www.nal.go.jp/strpc/eng/otl/hsfd/index.html)

National Space Development Agency of Japan, “CNES-NASDA Cooperation: A First Step Towards Reusable Launch Vehicles.”

[http://www.nasda.go.jp/Press/e/2000/200002/hope-x_000201_e.html]. February 2000.

Ray, Justin, “Pegasus Launch Report –HETE II.”

[<http://spaceflightnow.com/pegasus/hete2/status.html>]. October 2000.

NOAA S/T 76-1562. U.S. Standard Atmosphere.

Washington D.C. October 1976.

Space Daily, “HyShot Program Secures Place in Flight History.”

[<http://www.spacedaily.com/news/rocketscience-02v.html>]. August 2002.

Space and Tech, “Atlas III Summary.”

[http://www.spaceandtech.com/spacedata/elvs/atlas3_sum.shtml]. June 2001.

Soppet, Mark, “The Scramjet Revolution.”

[<http://www.geocities.com/xplanes2000/Aurora.html>]. April 2000.

University of Queensland, “HyShot- A University of Queensland Initiative.”

[<http://www.mech.uq.edu.au/hyper/hyshot/>]. October 2001.

USAF, “Standoff Hypersonic Missile with Attack Capability (SHMAC).”

[<http://www.au.af.mil/au/2025/volume3/chap12/v3c12-3.htm>]. August 1996.

USAF, “West Coast Offshore Operating Area (WCOOA).”

[<http://www.acq.osd.mil/te/mrtfb/commercial/sw30/wspace.html>]. January 1997.

Virginia Pilot, “Navy again delays the release of its F/A-18 impact statement.”

[http://www.jetnoise.org/va_pilot.htm]. March 2002.

Washington AFP, “Columbia Shuttle Launch Pushed Back Several Weeks.”

[<http://www.spacedaily.com/yesterday/spacedaily-2002-7.html>]. 26 June 2002.

Wertz, James R., "Economic Model of Reusable vs. Expendable Launch Vehicles,"
Paper presented at the IAF Congress, Rio de Janeiro, Brazil, 2-6 October 2000.

Whitmore, Stephen T., NASA, 28 March 2002.

BIBLIOGRAPHY

Isakowitz, Steven J., J.P. Hopkins Jr., J.B. Hopkins, International Reference Guide to Space Launch Systems, 3rd Edition, American Institute of Aeronautics and Astronautics, Inc. Reston, VA 1999.

Orbital Sciences Corporation, Pegasus User's Guide, Release 5.0, August 2000.

Sellers, Jerry Jon, Understanding Space: An Introduction to Astronautics, 2nd Edition, Mcgraw Hill, New York, NY 2000.

Vallado, David A., Fundamentals of Astrodynamics & Applications, 2nd Edition, Microcosm Press, El Segundo, CA 2001.

Wertz, James A., W.J. Larson, Space Mission Analysis and Design, 3rd Edition, Microcosm Press, El Segundo, CA 1999.

THIS PAGE INTENTIONALLY LEFT BLANK

INITIAL DISTRIBUTION LIST

1. Defense Technical Information Center
Ft. Belvoir, Virginia
2. Dudley Knox Library
Naval Postgraduate School
Monterey, California
3. Dr. Stephen T. Whitmore
NASA Dryden Flight Research Center
Edwards, California
4. Charles M. Racoosin
Naval Postgraduate School
Monterey, California
5. Joel R. Sitz
NASA Dryden Flight Research Center
Edwards, California
6. Griffin P. Corpening
NASA Dryden Flight Research Center
Edwards, California
7. Michael D. Schafer
Naval Postgraduate School
Monterey, California